Probing Accretion Turbulence in the Galactic Centre with EHT Polarimetry

by

Chunchong Ni

A thesis
presented to the University of Waterloo
in fulfillment of the
thesis requirement for the degree of
Master of Science
in
Physics

Waterloo, Ontario, Canada, 2018

I hereby declare that I am the sole author of this thesis. This is a true copy of the thesis, including any required final revisions, as accepted by my examiners.

I understand that my thesis may be made electronically available to the public.

Abstract

We explore the origin and the influence of the interstellar scattering on the observation of Sgr A*, and the method to mitigate this scattering via Event Horizon Telescope (EHT) polarimetry. Interstellar scattering is due to the existence of inhomogeneous plasma screens between the Earth and Sgr A*. At radio wavelengths, this scattering adds and removes small structures in the images. In the EHT observation, the scattering contaminates the image by moving power from long baselines to short baselines in a fashion that may be described by a linear transformation characterized by the Scattering Shift Kernel. However, for credible interstellar magnetic field strengths, this transformation is insensitive to polarization. Therefore, it is possible to distinguish intrinsic and scattered structures via the image power spectra constructed in different polarization components.

Via numerical experiments, we demonstrate a method for reconstructing intrinsic structure information. We do this for two cases: a toy model in which we show that this method accurately reproduces the characteristics of controlled image fluctuations, and general relativistic magnetohydrodynamic simulation images. Specifically, we show that the ratio of the power spectra obtained independently for different polarization components is independent of the scattering screen given the current observational limitations of the EHT. Therefore, these power spectra ratios provide a window directly into the magnetohydrodynamic turbulence believed to drive accretion onto black holes.

Acknowledgements

I would like to thank my supervisor Avery E. Broderick, who provides many suggestions on this thesis and the whole project, and Roman Gold, who provides the GRMHD simulation data and many thoughtful ideas, and many others who offer valuable opinions.

Dedication

This is dedicated to my friends and my family, who support me all the time.

Table of Contents

List of Tables

List of Figures

Chapter 1

Introduction

Black holes have been implicated as the engines of active galactic nuclei (AGN) and X-ray binaries [1]. Within these objects, both their extreme luminosities and growth rate are presumably due to the interaction with the accretion of nearby matter. This occurs via accretion disks, through which material orbits, cools and falls inward toward the central object. Accretion flows are generic features in astronomical systems, from the formation of planets to the powering of AGN, and thus understanding the processes by which they operate informs astrophysics broadly.

For material to move inward toward a central accreting mass, it must lose both energy and angular momentum. For geometrically and optically thick flows, the former can be a limiting factor. However, for AGN it is typically the latter, angular momentum, that is the practical barrier. Developing the ability to empirically access the processes responsible for transporting angular momentum through the accretion flow is the topic of this thesis.

There are few candidates to explain the angular momentum transport in the accretion disk. Molecular viscosity is ruled out, as the theoretical prediction of angular momentum transport rate is orders of magnitude lower than the observed rate [34, 31, 9]. It is currently widely believed that the main driver of angular momentum transfer is hydrodynamic viscosity caused by turbulence and magnetic stresses. Both of these are the result of magnetohydrodynamic (MHD) turbulence with accretion flows, presumably sourced by the magnetorotational instability [1].

Multiple numerical simulations of the MHD have been performed to study the properties of accretion flows dominated by magnetic viscosity [see, e.g., 28]. In the cases of accretion disks around the black holes, general relativity must be included due to the strong gravitational field. Yet, the general relativisitic MHD (GRMHD) simulations have

their own limitations, as all GRMHD simulation tests neglect the turbulence generated below the grid scale. Computation expense prevents simulations from resolving the Larmour scale, the presumptive dissipation scale within the physical system. The impact of this oversight remains unclear, as the turbulence generated at such small scales might influence the results drastically [29]. Thus, to testify the current GRMHD simulations, it remains necessary to develop empirical methods to probe the nature and properties of MHD turbulence near black holes.

The supermassive black hole at the Galactic Centre, Sagittarius A* (Sgr A*), offers us a laboratory in which to study accretion flows in detail. Sgr A* is located at the centre of the Milky Way, 8 kpc away from the Earth, with a mass of $4.3 \times 10^6\ M_\odot$ [11, 4, 14]. Being a strong, compact radio source, the study of Sgr A* presents an opportunity to test the theories of astrophysics under extreme conditions.

The Event Horizon Telescope (EHT) offers an unprecedented opportunity to observe the Galactic centre with sub-horizon resolution. The EHT is an international project comprised of a number of radio telescopes across the globe, aiming at probing the two supermassive black holes, Sgr A* and M87. Telescope sites are located in Hawaii (James Clerk Maxwell Telescope (JCMT), The Submillimeter Array (SMA)), North America (Arizona Radio Observatory/Submillimeter-wave Astronomy (ARO/SMT), The Large Millimeter Telescope (LMT)), Europe (Atacama Pathfinder EXperiment (APEX), IRAM 30-meter telescope), South America (Atacama Submillimeter Telescope Experiment (ASTE), Atacama Large Millimeter/Submillimeter Array (ALMA)) and Antarctica (South Pole Telescope (SPT)). The technique used by EHT is very long baseline interferometry (VLBI). By creating a virtual aperture of the size of the Earth with synthesized data from all of the telescope sites, the EHT is able to achieve a resolution of around 13 microarcseconds at a wavelength of 1.3 mm (230 GHz). In comparison, the typical angular size of the shadow for Sgr A* and M87 is 55 and 40 microarcseconds, respectively. With this resolution, it becomes possible to look into the accretion physics on scales comparable to those relevant for MHD turbulence. Two observing campaigns have been completed, in April 2017 and 2018, and analysis is underway. In both the full complement of Stokes parameters were measured at 230 GHz. Future development of the array will include the ability to observe at 345 GHz.

Sgr A* presents the primary horizon-scale science for the EHT. As the closest supermassive black hole to the Earth, it presents the largest shadow diameter in angular size. It is also believed to contain a thick, hot accretion disk. This presents a larger dynamic range of MHD turbulence phenomena (typically bounded on the largest scales by the disk height). Thus, it presents a natural target for studying MHD turbulence in astrophysical systems. Finally, it is optically thin, ensuring that turbulent features throughout the

accretion flow are visible, and simplifying their interpretation.

However, there are two practical difficulties with observing and characterizing MHD turbulence within the accretion flow of Sgr A*. First, gravitational lensing distorts the image of the innermost regions of the accretion flow. This may be modelled and corrected given the parameters of the central black hole [30, 10, 5, 21]. Second, interstellar scattering distorts the mm-wavelength images [8, 16, 18, 19]. This scattering is a stochastic effect caused by the fluctuations of electron density in the interstellar plasma, and the scattering effect can be modelled by a thin scattering screen. The existence of the scattering screen between the Earth and Sgr A* severely contaminates the observation in two different ways. First, the scattering adds and removes small structures. Second, the image is angularly broadened, scaling as λ^2. In EHT observations, there will be an excess power at long baselines consistent with refractive modes in the screen.

The nature and properties of the scattering screen are not yet fully understood. Most efforts assume a single screen, though this need not be the case. The single scattering screen model assumes the scattering medium causing the angular broadening of Sgr A* is located between the galactic centre and Earth [7]. Although we have an estimation of the size of the screen, which is $59 \pm 6\mu$as for the major axis and $60 \pm 30\mu$as for the minor axis, at 1.3 mm observational wavelength, any single realization of the fluctuations remain unconstrained [20]. That is, the parameters of the region responsible for scattering images of Sgr A* are poorly constrained, including the location and the structure of the scattering screen. As a result, it is not straightforward to model and remove the impact of this scattering from images of Sgr A*.

Quantitative models of the scattering region do exist, comprised of a statistical description of the fluctuations in the plasma density across a single screen [18]. In these, the turbulence in the scattering screen is generated at very small scales (as small as the size of the Earth) and varies on timescales of many hours. Efforts to constrain the screen properties have succeeded in modeling its behavior above 3mm [20]. These address the statistical structure of the scattering screen, i.e. the power law of the structure function of the scattering screen (one general guess is that the scattering screen is of Kolmogorov), as well as on the estimation of scale size where the turbulence is generated and damped.

Motivated by the current uncertainty in the screen parameters and structure, we present a novel way to mitigate the effect of interstellar scattering using polarization. The key physical input is that the scattering screen is both non-birefringent and linear. In Section 2.1, we present estimates of the birefringence of the screen given reasonable parameters for the interstellar medium. In Section 2.2, we review and extend the previous work done on the interstellar scattering by other research groups, namely laying out the mathematical

connection between the intrinsic and scattered power spectrum of the VLBI observables, and define the Scattering Shift Kernel (SSK) that characterizes this relationship. In Section 2.3, we explore the behaviour of the SSK, and why our application of non-birefringent nature of the screen is able to effectively mitigate the contamination from scattering.

Chapter 3 focuses on the numerical simulation and the analysis of the expected results of a toy model. Section 3.1 shows the step-by-step method of generating toy model images, with the designated polarizations. Section 3.2 presents the method by which we numerically simulate EHT observations, in which the scattering model is constructed and coded based on the EHT-imaging (EHTim) library by Andrew Chael, available at `https://github.com/achael/eht-imaging`. In Section 3.3, the analysis of the simulation results of the toy model is provided.

Chapter 4 shows the simulation results using GRMHD as the intrinsic source image. The structure of this chapter is parallel to Chapter 3. Sectio 4.1 sets up the GRMHD data and its feature, which is generated by Roman, McKinney et al. [12]. In Section 4.2, the same method of simulating the EHT observation is used upon GRMHD data as in Section 3.2. Section 4.3 provides the method to construct the special polarization modes based on the GRMHD simulation. Section 4.4 estimates the potential thermal noise and ensemble noise. Section 4.5 presents the analysis of the simulation results on different polarization modes of GRMHD data, parallel to Section 3.3. In the last section of this chapter, we further explore the reaction of significant variations in the properties of the scattering.

Finally, conclusions and future prospects are collected in Chapter 5.

Chapter 2

Scattering and Observation of Polarized Light

2.1 Limits on the Birefringence of Scattering in the ISM

The current model for the interstellar scattering is that the scattering is caused by density fluctuations in the interstellar medium, whose impact is abstracted as a scattering screen that adds a random phase factor to the incoming signals at different locations [22, 13]. So far, this model reproduces the observed scattering of Sgr A* well [27]. Yet, for the case of Sgr A*, uncertainty regarding the number and location of the scattering screens exists, as well as their structure [7]. In this thesis, we will neglect the possibility of multiple screens and hold the screen fixed between the Earth and Sgr A* (in the numerical experiments in this thesis, the screen is put $2.82kpc$ away from the Earth and $5.53kpc$ away from Sgr A*). The reasons are twofold: simplicity and if our argument holds true for one screen, we would be able treat multiple screens in a similar manner.

We begin by showing that, for reasonable conditions within the interstellar medium, the scattering must be non-birefringent, i.e., does not treat different polarization modes differently. Note that this does not mean that the substructure induced by scattering in images made in different polarizations are identical; this substructure depends on the structure of the intrinsic image. Rather, it implies that the linear transformation between the intrinsic image and the scattered image is identical for all polarization modes. The key idea is to exploit the lack of birefringence in the scattering screen to leverage both

polarized and unpolarized observations to construct a scattering-independent measure of turbulence in the source.

The dispersion relation for the electromagnetic waves at a plasma background with magnetic field is:

$$k_{\pm}^2 c^2 = \omega^2 - \omega_P^2 \pm \omega_P^2 \frac{\omega_B}{\omega}, \tag{2.1}$$

where $\omega_P^2 = 4\pi e^2 n/m_e$ is the plasma frequency, and $\omega_B = eB/m_e c$ is the cyclotron frequency. By defining $X = \omega_P^2/\omega^2$ and $Y = \omega_B/\omega$, we can solve for the momentum, k, as a function of ω, X and Y.

$$k_{\pm} = \frac{\omega}{c}\sqrt{1 - X \pm XY}. \tag{2.2}$$

In the first order approximation, as $\omega \gg \omega_P, \omega_B$,

$$k_{\pm} \approx \frac{\omega}{c}\left(1 - \frac{1}{2}X \pm \frac{1}{2}XY\right). \tag{2.3}$$

The impact of the scattering on the electromagnetic wave is that the screen adds an extra phase to it. The phase delay, ϕ, due to the scattering screen, is:

$$\phi = Lk - L\frac{\omega}{c}, \tag{2.4}$$

where L is the physical scale of the scattering screen, as illustrated in Fig. 2.1. Thus, the phase delay due to the scattering screen for different polarization modes, k_+ and k_-, is:

$$\phi_{\pm} = -\frac{1}{2}\frac{\omega}{c}XL \pm \frac{1}{2}\frac{\omega}{c}XYL. \tag{2.5}$$

The first term, $-\omega XL/2c$, is the residual phase delay even without the background magnetic field; therefore, we define this term as $\phi_0 = -\omega XL/2c$. Under this notation, the phase delay can be described in terms of two variables, ϕ_0 and Y:

$$\phi_{\pm} = \phi_0\left(1 \pm Y\right). \tag{2.6}$$

The difference in the phase delay due to the scattering screen for different polarization modes is:

$$\phi_+ - \phi_- = 2\phi_0 Y. \tag{2.7}$$

To assess the magnitude of this phase difference, and thus address the birefringence of the scattering screen, it is necessary to compute Y (which depends solely on magnetic field strength and is generally small) and ϕ_0. To find ϕ_0, we relate the magnitude of the

phase shift to the refraction of radio waves through the screen, and therefore the size of the diffractive component, which is well measured. The dispersion relationship for the electromagnetic waves at a plasma background in the absence of a magnetic field is:

$$\omega^2 = k^2c^2 + \omega_P^2. \tag{2.8}$$

Hamilton's equations connect the time-evolution of position and momentum with the energy and the momentum:

$$\begin{aligned} \frac{dx}{dt} &= c, \\ \frac{dk}{dt} &= -\nabla\omega(k, x). \end{aligned} \tag{2.9}$$

Considering an electromagnetic plane wave initially propagating along the x-axis that after passing through the scattering screen is deflected in the y-axis, in the weak deflection limit, justified by the small scattering angles observed (<10 μas at 1.3 mm), we can estimate the refraction angle:

$$\theta = \frac{\Delta k_y}{k_x}. \tag{2.10}$$

In the x-axis, if we expand Equation 2.9 with the dispersion relationship, and adopt the assumption that the electron density remains close before and after scattering, the following approximation can be applied, up to the first-order correction:

$$\frac{dk_x}{dt} = -\frac{1}{2\omega}\frac{\partial}{\partial x}\omega_P^2 \tag{2.11}$$

$$= -\frac{\omega_P^2}{2\omega}\frac{\partial}{\partial x}\ln n \tag{2.12}$$

$$\approx -\frac{\omega_P^2}{2\omega}\frac{1}{L}. \tag{2.13}$$

In the y-axis, as the scattering screen is isotropic, the derivative of k_y over time follows the same relation as k_x:

$$\frac{dk_y}{dt} = -\frac{\omega_P^2}{2\omega}\frac{1}{L}. \tag{2.14}$$

The derivative of k_y along the direction of propagation is:

$$\frac{dk_y}{dx} = \frac{\dot{k}_y}{\dot{x}} \tag{2.15}$$

$$= -\frac{\omega_P^2}{2\omega c}\frac{1}{L}. \tag{2.16}$$

Thus, the change of momentum perpendicular to the direction of propagation is

$$\Delta k_y = \int dx \frac{dk_y}{dx} = -\frac{\omega_P^2}{2\omega c}. \tag{2.17}$$

Thus, the refraction angle due to scattering is

$$\theta = \frac{\Delta k_y}{k_x} = -\frac{1}{2}X. \tag{2.18}$$

In reality, we already have an idea what the value of θ is, as it is a function of the observational wavelength λ. For Sgr A*, the scattering kernel is anisotropic. The minor axis of the scattering kernel is approximately half the size of the major axis. As we are only making an estimate of the refraction angle, it is sufficient to adopt either one of the two axes. For example, the refraction angle in the direction of the major axis in the unit of micro-arcsecond is:

$$\theta \approx 1.309\left(\frac{\lambda}{1\text{ cm}}\right)^2 \text{ mas}. \tag{2.19}$$

Knowing the refraction angle θ, we can estimate the phase delay, ϕ_0, in terms of the ratio of ω_P^2 and ω, X, and the physical size of the scattering screen, L. For X, it is easy to make a direct calculation from Equation 2.18. For the physical size of the scattering screen, if we take the assumption that the scattering screen is 2 kpc away from us, the upper limit for the physical size of the scattering screen would be

$$L \leq \theta D, \tag{2.20}$$

where D is the distance from the scattering screen to us.

For sub-milimetre observations, under the conditions that the scattering screen is located 2 kpc away and there is no background magnetic fields, the phase delay is calculated up to the first order approximation:

$$\phi_0 = -\frac{1}{2}\frac{\omega}{c}XL \approx 20. \tag{2.21}$$

Therefore, for the case when a background magnetic field is present, the difference between phase delays in the two different polarization modes is:

$$\phi_+ - \phi_- = 2\phi_0 Y = 2 \times 10^{-9}\left(\frac{B}{\mu G}\right). \tag{2.22}$$

In general, $\phi_+ - \phi_- \ll 2\pi$, with an ordinary interstellar magnetic field. Thus, we can conclude that the difference in the phase delay of two polarization modes is small, whereas the non-birefringence feature holds true with the ordinary interstellar magnetic field.

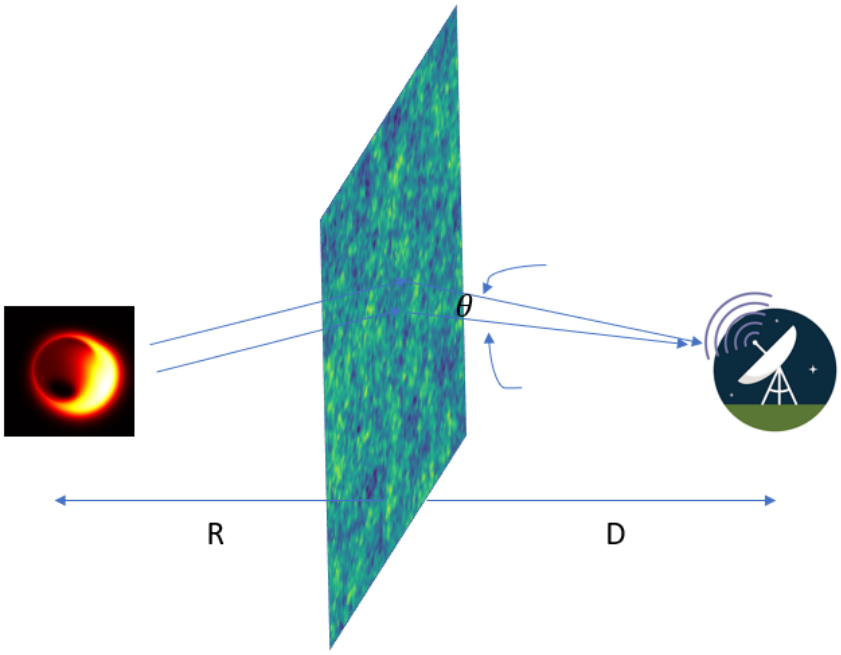

Figure 2.1: The scattering screen is put at distance R to Sgr A*, and distance D to the Earth. The scattering screen is generated through the fluctuation of electrons. Two parallel radiations of different polarization modes from Sgr A* travel through the scattering screen, and undergo the refraction caused by the scattering screen. The difference of the refraction angle between these two polarization modes, θ, is tiny under any credible interstellar magnetic field.

2.2 Polarization in the Scalar Light Approximation

Instead of using electromagnetic waves, we apply the scalar light approximation. The benefit of this scalar light approximation is that we are able to retain the propagation property of the electromagnetic wave, while the calculation is simplified. Although we lose the ability to express the polarization information in one wave amplitude function, we are able to recover the polarization information with multiple independent scalar electric fields, as different modes of polarizations (both left-handed and right-handed) can be described by separate scalar fields. Thus, the scalar light approximation is good enough at capturing the key features of scattering. In this subsection, we are going to review the interstellar scattering of Sgr A* with the scalar light approximation. We will see that the non-birefringence feature discussed in the previous subsection plays an important role in mitigating the interstellar scattering of Sgr A*.

Thus, we can write down the scalar electric field If we consider an extended intrinsic source, $\Psi_{int}(\mathbf{s})$, where $\mathbf{s}$ is the transverse coordinate in the source plane, we are able to calculate calculate the scalar electric field $\Psi(\mathbf{b})$ after scattering, where $\mathbf{b}$ is the EHT baseline coordinate, via the Huygens-Fresnel principle [15, 22, 13]. According to the Huygens-Fresnel principle, both the emission in the source and at the scattering screen are decomposed into spherical wavelets, which are then summed to produce the electric field at the observer, integrating over both the extended radiation source and the scattering screen plane. We can apply the far field approximation, and thus the integral can be approximated by a twofold Fourier transform of the intrinsic source, $\Psi_{int}(\mathbf{s})$. The geometry of the problem is shown in Fig. 2.1. The expression for the interstellar scattering is:

$$\Psi_{scatt}(\mathbf{b}) = \frac{1}{2\pi r_F^2} \int d^2\mathbf{x} e^{i[k/(2D)|\mathbf{b}-\mathbf{x}|^2+\phi(\mathbf{x})]} \int d^2\mathbf{s} e^{i[k/(2R)]|\mathbf{x}-\mathbf{s}|^2} \Psi_{int}(\mathbf{s}). \tag{2.23}$$

Here, $\phi(\mathbf{x})$, a Gaussian random variable with zero-mean value, is the extra phase factor from the scattering screen at location $\mathbf{x}$ in the scattering screen plane. The screen is placed at the distance D from the Earth and distance R to the galactic centre, and r_F is the Fresnel scale. The Fresnel scale, defined by following equation, quantifies the extra phase delay due to the geometry of observation.

$$r_F \equiv \sqrt{\frac{DR}{D+R}\frac{1}{k}}, \tag{2.24}$$

where $k = 2\pi/\lambda$ is the wavenumber of the scalar electric field, and λ is tits wavelength of our observing waveband.

The chief observable in radio astronomy is the visibility, also known as the correlated flux density. The visibility is the expectation value of the product of electromagnetic fields at two different locations connected by the given baseline, which is centred at $\mathbf{r}$

$$V(\mathbf{b},\mathbf{r}) = \left\langle \Psi_{scatt}\left(\mathbf{r}-\mathbf{b}/2\right)\Psi^{*}_{scatt}\left(\mathbf{r}+\mathbf{b}/2\right)\right\rangle. \tag{2.25}$$

Similarly, the definition of the total intensity is given by the product of the electromagnetic fields at the same location, $I\left(\mathbf{b}\right) = \left\langle \Psi_{scatt}\left(\mathbf{b}\right)\Psi^{*}_{scatt}\left(\mathbf{b}\right)\right\rangle$. With Van Cittert-Zernike Theorem, the intensity and the visibility are connected with Fourier transformation [36]. For the intrinsic source, adopting the incoherence property, the intrinsic total intensity and the intrinsic visibility is:

$$I\left(\mathbf{s},\mathbf{s}'\right)\delta(\mathbf{s}-\mathbf{s}') = \left\langle \Psi_{scatt}\left(\mathbf{s}\right)\Psi^{*}_{scatt}\left(\mathbf{s}'\right)\right\rangle. \tag{2.26}$$

$$V_{int}[\,(\,1+M)\,(\,\mathbf{x}_2-\mathbf{x}_1)\,] \;= \int d^2\mathbf{s}e^{ik/R(\mathbf{x}_2-\mathbf{x}_1)\cdot\mathbf{s}}I_{int}(\mathbf{s}), \tag{2.27}$$

where $M = D/R$. Thus, the visibility domain and image domain can be connected through the Fourier transformation.

If we construct the coordinate system such that the baseline is centred at zero in the coordinate system, i.e. $\mathbf{r}=0$, the visibility of a given baseline $\mathbf{b}$ is the product two electric fields at $\mathbf{b}/2$ and $-\mathbf{b}/2$ from Equation 2.23:

$$\begin{aligned} V(\mathbf{b}) &= \left\langle \Psi_{scatt}\left(-\mathbf{b}/2\right)\Psi^{*}_{scatt}\left(\mathbf{b}/2\right)\right\rangle \\ &= \frac{1}{4\pi^2 r_F^4}\int d^2\mathbf{x}_1 d^2\mathbf{x}_2 \\ &\times e^{i/2r_F^{-2}[\,(\,\mathbf{x}_1^2-\mathbf{x}_2^2)+\mathbf{b}/(1+M)(\,\mathbf{x}_1+\mathbf{x}_2)\,]} \\ &\times \left\langle e^{i[\,\phi(\,\mathbf{x}_1)-\phi(\,\mathbf{x}_2)\,]}\right\rangle V_{int}[\,(\,1+M)\,(\,\mathbf{x}_2-\mathbf{x}_1)\,]. \end{aligned} \tag{2.28}$$

Note that there are two sources of variability due to refraction in the scattering screen. One is the variability of the scattering screen, the other is the variability of the source. The expression above is the average over both the variabilities, as both the scattering screen and the radiating source vary on a timescale of hours. For each observational night, we would have several independent snapshots of the visibility. Yet, what we are interested in is the statistical structure of the intrinsic visibility of the source, which encodes the physics of the disk turbulence around Sgr A*. If we are to explore the behaviour of the visibility in

the ensemble average regime, i.e., the average over many realizations of both the scattering disk and the source, we need to describe the statistical structure of the scattering screen.

The Gaussianity feature of $\phi(\mathbf{b})$ gives a convenient identity:

$$\left\langle e^{i[\,\phi(\,\mathbf{x}_1)-\phi(\,\mathbf{x}_2)\,]}\right\rangle = e^{-1/2\left\langle[\phi(\mathbf{x}_1)-\phi(\mathbf{x}_2)]^2\right\rangle}. \tag{2.29}$$

The average over the scattering screen is described the structure function, D_ϕ, whose definition is:

$$D_\phi(\mathbf{x}_1-\mathbf{x}_2) = \left\langle\left[\phi(\mathbf{x}_1)-\phi(\mathbf{x}_2)\right]^2\right\rangle. \tag{2.30}$$

The detailed information of this structure function is going to be discussed in the next section, but if we apply this definition to Equation 2.28, we will have an expression for the ensemble average of the scattered visibility:

$$\langle V_{scatt}(\,\mathbf{b})\,\rangle_{ea,turb} = e^{-D_\phi(\,\mathbf{b}/(1+M))}\,\langle V_{src}(\,\mathbf{b})\,\rangle_{ea,turb}, \tag{2.31}$$

as well as the ensemble average of the averaged visibility squared:

$$\begin{aligned}\langle\!|V_{scatt}|^2\,(\,\mathbf{b})\,\rangle_{ea,turb} = \frac{1}{(\,2\pi r_F^2)^{\,2}}\int d^2\mathbf{u}d^2\mathbf{z}\times e^{ir_F^{-2}[\,\mathbf{u}+(\,1+M)^{\,-1}\mathbf{b}]\cdot\mathbf{z}}\\ \times\, e^{-1/2[\,2D_\phi(\,\mathbf{z})+2D_\phi(\,\mathbf{u})-D_\phi(\,\mathbf{u}+\mathbf{z})-D_\phi(\,\mathbf{z}-\mathbf{u})\,]}\\ \times\,\langle\!|V_{int}|^2\,[\,(\,1+M)\,\mathbf{u}]\,\rangle_{ea,turb},\end{aligned} \tag{2.32}$$

which we will refer to as appropriate as the "power spectrum" of the image as it encodes in a statistical fashion the variations in the image structure.

Conventionally, the structure function is assumed to be quadratic [13, 15]. Under this assumption, the two equations above can be further simplified. For Equation 2.32, the exponent, $2D_\phi(\mathbf{z})+2D_\phi(\mathbf{u})-D_\phi(\mathbf{u}+\mathbf{z})-D_\phi(\mathbf{z}-\mathbf{u})$, becomes zero; thus, the exponential term, $e^{-1/2[\,2D_\phi(\,\mathbf{z})+2D_\phi(\,\mathbf{u})-D_\phi(\,\mathbf{u}+\mathbf{z})-D_\phi(\,\mathbf{z}-\mathbf{u})\,]}$, becomes one, and the rest part of the integral can be done analytically, which gives:

$$\langle\!|V_{scatt}|^2\,(\,\mathbf{b})\,\rangle_{ea,turb} = \langle\!|V_{int}|^2\,(\,\mathbf{b})\,\rangle_{ea,turb}. \tag{2.33}$$

Since the scattering screen is non-birefringent, if we take the ratio of the different power spectra of different polarization modes, we should be able to retrieve some intrinsic information from the ratio of the scattered power spectra:

$$\frac{\left\langle\left|V_{scatt}^{L_1}(b)\right|^2\right\rangle}{\left\langle\left|V_{scatt}^{L_2}(b)\right|^2\right\rangle} = \frac{\left\langle\left|V_{int}^{L_1}(b)\right|^2\right\rangle}{\left\langle\left|V_{int}^{L_2}(b)\right|^2\right\rangle}. \tag{2.34}$$

Here, both the power spectrum and the variance have the statistical information, yet our choice of the power spectrum as the averaged visibility squared is made based on the desire to construct a quantity that may be robustly related to the intrinsic properties of the image. Instead, if the ratio of different variances is taken, even for an ideal (quadratic) structure function, the ratio for intrinsic variance does not equal to the ratio of the scattered ones:

$$\frac{\Sigma^2_{L_1}}{\Sigma^2_{L_2}} = \frac{\sigma^2_{L_1} + \left(1 - e^{-b^2/(1+M)^2 r_0^2}\right)\left\langle V^{L_1}_{int}(\mathbf{b})\right\rangle}{\sigma^2_{L_2} + \left(1 - e^{-b^2/(1+M)^2 r_0^2}\right)\left\langle V^{L_2}_{int}(\mathbf{b})\right\rangle}, \tag{2.35}$$

where L_1 and L_2 are two different polarization modes (the detailed calculation of this quantity is shown in the Appendix).

If the approximation that the structure function is quadratic is relaxed, the exponential term in Equation 2.32 no longer vanishes. Therefore, the integral may no longer be solved analytically. For the exponent, $2D_\phi(\mathbf{u}) + 2D_\phi(\mathbf{z}) - D_\phi(\mathbf{u}+\mathbf{z}) - D_\phi(\mathbf{z}-\mathbf{u})$, the last three terms reduce to the second-order derivative of $D_\phi(\mathbf{z})$ when $|\mathbf{u}|$ is much smaller than $|\mathbf{z}|$. Thus, if we define the scattering Scattering Shift Kernel (SSK) as:

$$K(\mathbf{u},\mathbf{b}) = \frac{1}{(2\pi r_F^2)^2}\int d^2\mathbf{z} e^{i r_F^{-2}\mathbf{z}(\mathbf{u}+\mathbf{b}/(1+M))}\frac{1}{2}\mathbf{u}^2 D''_\phi(\mathbf{z}), \tag{2.36}$$

we are able to separate Equation 2.32 into two different parts, one with the integral of the SSK and the other independent of the SSK:

$$\langle |V_{scatt}|^2(\mathbf{b})\rangle = e^{-D_\phi(-\mathbf{b}/(1+M))}\langle |V_{int}|^2(\mathbf{b})\rangle + \int d^2\mathbf{u} K(\mathbf{u},\mathbf{b}) e^{-D_\phi(\mathbf{u})}\langle |V_{int}|^2[(1+M)\mathbf{u}]\rangle. \tag{2.37}$$

The first term here is proportional to the intrinsic power spectrum, and the second term is the correction from scattering through the SSK.

2.3 Scattering Shift Kernel and its Properties

From the previous two sections, we have reached two conclusions: the scattering screen is well-approximated as being non-birefringent, and the scattered power spectrum is a function of the intrinsic power spectrum plus a correction from the integration over the SSK. Therefore, the ratio of the image power spectra for two different polarization components

is generally,

$$\frac{\left\langle \left| V_{scatt}^{L_1}(\mathbf{b}) \right|^2 \right\rangle}{\left\langle \left| V_{scatt}^{L_2}(\mathbf{b}) \right|^2 \right\rangle} = \frac{e^{-D_\phi(-\mathbf{b}/(1+M))} \left\langle \left| V_{int}^{L_1} \right|^2 (\mathbf{b}) \right\rangle + \int d^2\mathbf{u} K(\mathbf{u},\mathbf{b}) e^{-D_\phi(\mathbf{u})} \left\langle \left| V_{int}^{L_1} \right|^2 [(1+M)\mathbf{u}] \right\rangle}{e^{-D_\phi(-\mathbf{b}/(1+M))} \left\langle \left| V_{int}^{L_2} \right|^2 (\mathbf{b}) \right\rangle + \int d^2\mathbf{u} K(\mathbf{u},\mathbf{b}) e^{-D_\phi(\mathbf{u})} \left\langle \left| V_{int}^{L_2} \right|^2 [(1+M)\mathbf{u}] \right\rangle}, \tag{2.38}$$

where L_1 and L_2 are the two different polarization modes and can be any linear combinations of the four Stokes parameters, (I, Q, U, V).

If in the SSK, the second-order derivative is a constant, i.e., the structure function D_ϕ is quadratic, then the problem becomes trivial: $K(\mathbf{u},\mathbf{b})$, becomes proportional to the Dirac-delta function, and the second term in Equation 2.37 can be integrated analytically (see Equation 2.39). Thus, the two terms on the right-hand-side of Equation 2.37 can be grouped together, and the ratio of power spectra is identical before and after scattering:

$$K(\mathbf{u},\mathbf{b}) \sim \delta\left(\mathbf{u} + \frac{\mathbf{b}}{1+M}\right) \frac{1}{2}\mathbf{u}^2 \tag{2.39}$$

$$\begin{aligned}
\frac{\left\langle \left| V_{scatt}^{L_1}(\mathbf{b}) \right|^2 \right\rangle}{\left\langle \left| V_{scatt}^{L_2}(\mathbf{b}) \right|^2 \right\rangle} &= \frac{e^{D_\phi[-\mathbf{b}/(1+M)]}[1 + \mathbf{b}^2/2(1+M)^2] \left\langle \left| V_{int}^{L_1}(\mathbf{b}) \right|^2 \right\rangle}{e^{D_\phi[-\mathbf{b}/(1+M)]}[1 + \mathbf{b}^2/2(1+M)^2] \left\langle \left| V_{int}^{L_2}(\mathbf{b}) \right|^2 \right\rangle} \\
&= \frac{e^{D_\phi[-\mathbf{b}/(1+M)]} e^{D_\phi[\mathbf{b}/(1+M)]} \left\langle \left| V_{int}^{L_1}(\mathbf{b}) \right|^2 \right\rangle}{e^{D_\phi[-\mathbf{b}/(1+M)]} e^{D_\phi[-\mathbf{b}/(1+M)]} \left\langle \left| V_{int}^{L_2}(\mathbf{b}) \right|^2 \right\rangle} \\
&= \frac{\left\langle \left| V_{int}^{L_1}(\mathbf{b}) \right|^2 \right\rangle}{\left\langle \left| V_{int}^{L_2}(\mathbf{b}) \right|^2 \right\rangle},
\end{aligned} \tag{2.40}$$

and Equation 2.40 recovers Equation 2.33.

The other trivial case is when the second term in Equation 2.37 is small. In that case, the second term in Equation 2.37 becomes secondary compared to the first term and negligible. Thus, the first term dominates, and the ratio between different power spectra is the same before and after scattering:

$$\frac{\left\langle \left| V_{scatt}^{L_1}(\mathbf{b}) \right|^2 \right\rangle}{\left\langle \left| V_{scatt}^{L_2}(\mathbf{b}) \right|^2 \right\rangle} \approx \frac{e^{D_\phi(-b)} \left\langle \left| V_{int}^{L_1}(\mathbf{b}) \right|^2 \right\rangle}{e^{D_\phi(-\mathbf{b})} \left\langle \left| V_{int}^{L_2}(\mathbf{b}) \right|^2 \right\rangle}. \tag{2.41}$$

These two cases correspond to two independent features of the scattering. The ratio of power spectrum will remain unchanged even after scattering, if the scattering screen is ideal with the quadratic structure function, or the magnitude of the intrinsic power spectrum is small. Note that the latter illustrates that the SSK shifts power among different baselines. This property is going to be used in the following Chapters to optimize power spectra ratios that employ constructed polarization modes.

The SSK is a direct function of D_ϕ, and where $D_\phi(x) \propto x^2$ is trivial. This is generally true for small argument (i.e., short baselines). Frequently, D_ϕ is characterized by the power spectrum of phase delays due to the scattering screen, i.e.,

$$Q_q \equiv \left|\phi_q\right|^2 \quad \text{where} \quad \phi_q \equiv \int_{-\infty}^{\infty} e^{-2\pi i q x}\phi(x)dx, \tag{2.42}$$

where ϕ_q is the Fourier transform of the phase delay field. These two descriptions are related through van Cittert-Zernike theorem, if we introduce a two-point correlation function R(x):

$$\begin{gathered} R(x) \equiv \langle \phi(y+x)\phi(y)\rangle \quad \text{thus} \quad D_\phi(x) = 2(R(0) - R(x)) \\ \text{where} \quad R(x) = \int dq e^{2\pi i q x} Q_q. \end{gathered} \tag{2.43}$$

The integral limit in Equation 2.43 is determined by two scales, the inner scale and the outer scale. The inner scale, r_{in}, is the scale where the turbulence is generated, while the outer scale, r_{out}, is the scale where the turbulence is damped. Under Fourier transform, the corresponding limit in q is $q_{max} = 2\pi/r_{in}$ and $q_{min} = 2\pi/r_{out}$. There are two limits, first of which is when the physical scale is between the inner and outer scale. In this case, the scattering becomes isotropic and the structure function follows the power law, $D_\phi(x) \sim |x|^\alpha$. The scattering parameter α usually takes the Kolmogorov value, i.e., $\alpha = 5/3$, but recently it has been suggested the value of α can be smaller than Kolmogorov [20]. In the second limit where the inner scale is much larger than the actual physical sizes we are interested in, i.e., $|r| \ll r_{in}$, then the Fourier phase is much less than 1, namely $2\pi q x \ll 1$. Therefore, we may Taylor expand the Fourier phase:

$$e^{2\pi i q x} \approx 1 + 2\pi i q x - 4\pi^2 q^2 x^2. \tag{2.44}$$

If we insert the above equation to back to acquire the structure function $D_\phi(x)$:

$$D_\phi(x) \approx 8\pi^2 x^2 \int_{q_{min}}^{q_{max}} dq q^2 Q_q. \tag{2.45}$$

Therefore, in the case where the inner scale is larger than the actual physical scale (projected baseline length onto the screen), the structure function is indeed quadratic. When the physical scale is larger than the inner scale, the structure function follows a power law, whose power is smaller than two. This result is illustrated in Fig. 2.2 for two different scattering screen models with different inner scale values. Thus, when the physical scale is within the inner scale, the ratio of the scattered power spectrum should be the same as the ratio of the intrinsic power spectrum, as the structure function is quadratic. We will further discuss the influence of the size of the inner scale on the power spectrum ratio in Chapter 4.6.2.

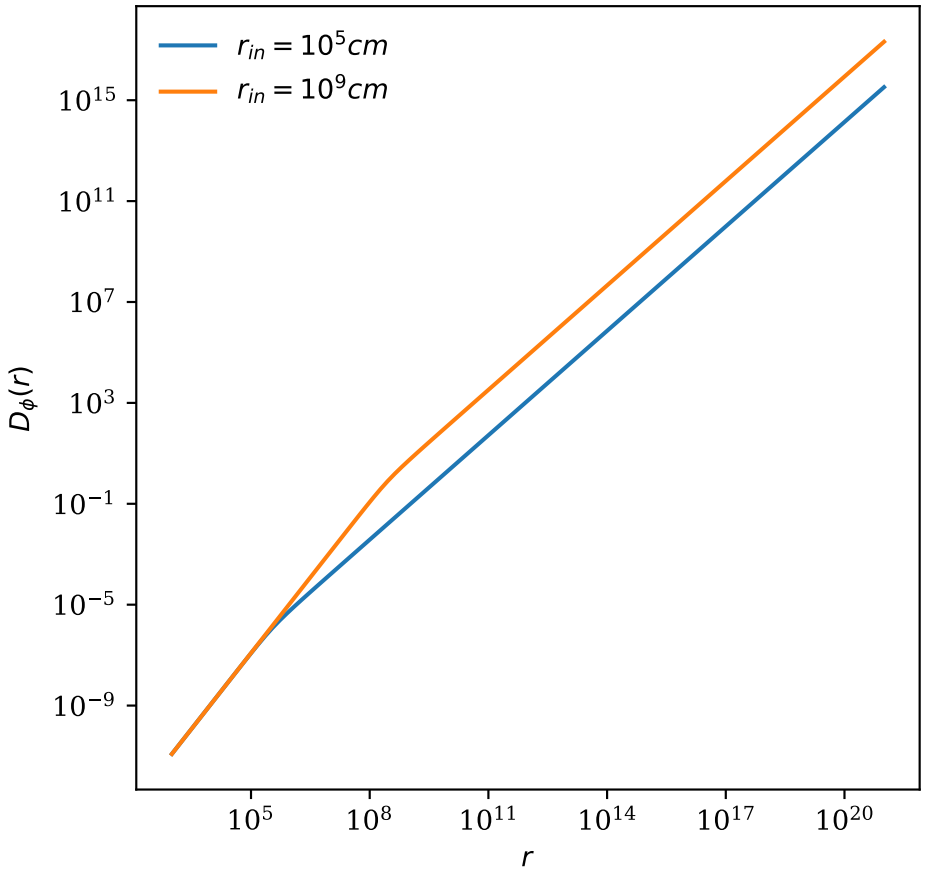

Figure 2.2: The structure function $D_\phi(r)$. When the physical scale is smaller than the inner scale, $D_\phi(r)$ is quadratic, while the physical scale is larger than the inner scale, $D_\phi(r)$ follows an isotropic power law. In this plot, we choose the index to be Kolmogorov and show different values of the inner scale.

Chapter 3

Reconstructing Intrinsic Structure: Toy Model

3.1 Constructing Structured Intrinsic Images

To explore how well the ratios between scattered power spectra of different polarization modes introduced in Chapter 2 encode the structure of the intrinsic ratios, i.e., before the imposition of additional structure due to refractive scattering, we construct a set of toy models. These toy models must satisfy a number of requirements: First, the model must generate predictions for the total intensity and multiple polarizations. Second, it must exhibit the typical scales anticipated in forthcoming EHT images of Sgr A*. Third, it must be able to accommodate a variety of distinct random fluctuations, i.e., with a number of differing intrinsic power spectra.

The intrinsic intensity without fluctuations is simulated by a Gaussian distribution:

$$\bar{I}(x, y) = I_0 e^{-(x^2+y^2)/2\sigma^2}, \tag{3.1}$$

where σ, the variance of the Gaussian distribution, is chosen to reproduce the typical scale of 1.3mm images of Sgr A*. In our toy model case, we choose the typical image size to be $24.4M$, and the corresponding σ for the Gaussian distribution is 1. The reason of choosing this size for the toy model is that this size is close to the physical size of Sgr A*. In making the picture from this Gaussian distribution, we choose 152 pixels in each axis. Similarly, the value of I_0 is chosen to present the total flux as a simulation to the total intensity of Sgr A* at 1.3mm wavelength. Confining both I_0 and σ, the requirements needed to exhibit the typical EHT total intensity and image scale at 1.3mm are fulfilled.

The next step is to add distinct random fluctuations to the Gaussian distribution above, to which a Gaussian random field component, $g(x, y)$ is added. The Gaussian random field, $g(x, y)$ has the power spectrum:

$$P_g(k, l) = N_\alpha u_{kl}(k^2 + l^2 + 1)^{\alpha/2}, \tag{3.2}$$

where k and l are the two-dimensional spatial frequencies in the sky, covering the whole range of image size of the toy models. u_{kl} is a Gaussian distribution independent from $\bar{I}(x, y)$. N_α is the normalization value for the power spectra. The choice of N_α is set such that the RMS fluctuation has an amplitude of $0.1I_0$, creating a uniform set of models differing only in the structure of the fluctuations. α is the power index which determines the colour of the power spectra. Blue power spectrum has more fluctuations at large frequencies, while red power spectrum has the more fluctuations at small frequencies. With positive αs, the colour of the power spectra are blue, i.e. the toy model would have many fluctuations at larger spatial frequencies. Similarly, the red power spectra are with negative αs, and the fluctuations mainly reside at shorter wavelengths for the toy model. The factor of 1/2 in the power index is for numerical calculation reason. Similarly, the $'' + 1''$ in the bracket comes from algorithmic consideration such that $k^2 + l^2 + 1$ is always larger than zero. Otherwise, when α is negative, the power spectrum P_g is not well-defined.

In this definition of the Gaussian random field, $g(x, y)$, with the given power spectrum, the Gaussian random field is the real part of the 2-dimensional Fourier transform of a Gaussian random distribution with power spectrum P_g:

$$g(x, y) = Re\ [\sum_{k,l}(P_g(k, l))^{1/2} e^{ikx+ily}\ ]. \tag{3.3}$$

Then, the intrinsic intensity with fluctuation is the Gaussian random distribution without fluctuation, $\bar{i}(x, y)$, multiplied by the exponential of the Gaussian random field, $g(x, y)$:

$$I(x, y) = \bar{I}(x, y)e^{-g(x,y)}. \tag{3.4}$$

Typically, the value of the Gaussian random field, $g(x, y)$ is small, as the normalization factor, N_α, is chosen to be small. Therefore, the definition of $I(x, y)$ is equivalent to being $I(x, y) = \bar{I}(x, y)[1 - g(x, y)]$.

There are a few parameters controlling the the shape of our simulated total intensity. First, we could change the size of the original Gaussian distribution through σ, which changes the size of the image. Second, we could change the normalization factor N_α, depending on the RMS fluctuation of the Gaussian random distribution, i.e. how much

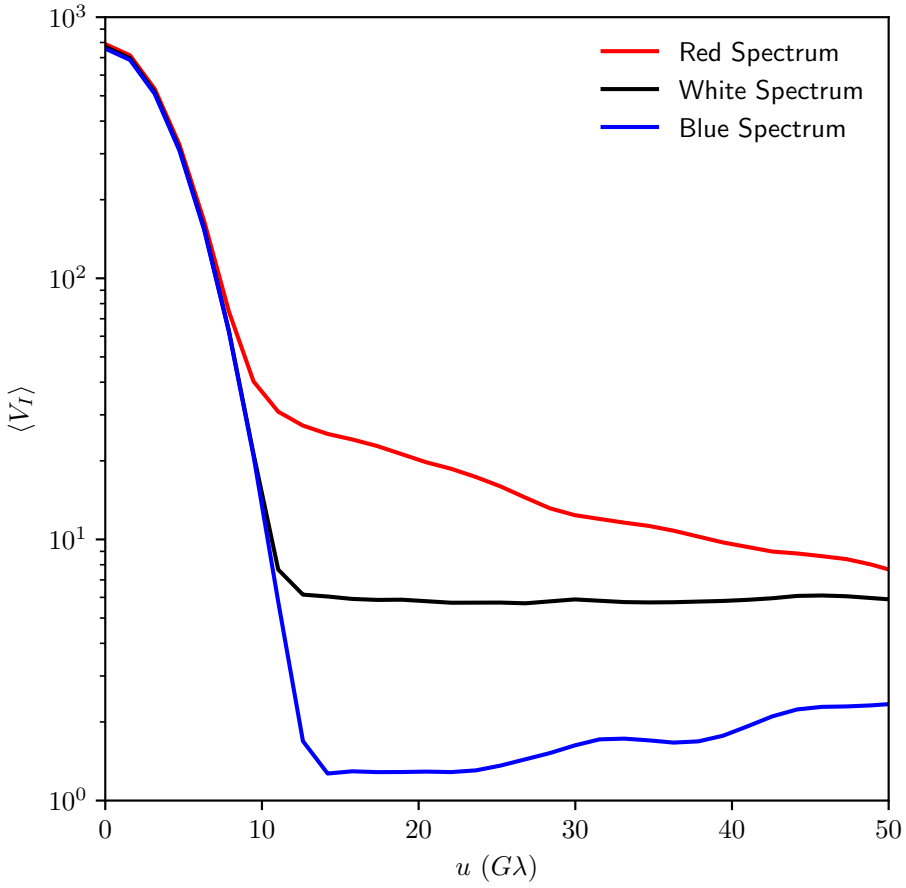

Figure 3.1: The power spectra for the toy models with different fluctuations. The red, blue and black lines represent different power spectra of fluctuation, whose features are manifested in the tail of the power spectra. It can also be noted that the total flux of these three power spectra is the same, as the value at zero, $\langle |V(0)| \rangle$ is the same.

fluctuation is needed. Last, and the most important, is α, which controls different types of the power spectrum of the Gaussian random field. Fig. 3.1 below shows the behaviour of the intrinsic intensity with different power spectra. In Fig. 3.1, the central bump is from the background Gaussian distribution, $\bar{I}(x, y)$, as the average value of the Gaussian distribution is non-zero. In the tails, the shapes follow the anticipated shapes from the Gaussian random field, $g(x, y)$, in which the red, white and blue spectrum corresponds to less fluctuation, no fluctuation and more fluctuation at long baselines respectively. Note that 50 Gλ is really large, whereas the EHT observation limit is about 10 Gλ; thus, the visibility is largely dominated by the background Gaussian at short baselines.

With a given I(x,y) we construct polarized images by specifying a polarization fraction. To simulate the polarization fraction we construct another independent Gaussian random field $g_L(k, l)$, from which the polarized image is obtained via

$$L(x, y) = I(x, y)g_L(x, y), \tag{3.5}$$

where $g_L(x, y)$ is an independent Gaussian random field. The independence depends on the independent construction of the power spectrum and its corresponding fluctuation, whose definition is similar to P_g:

$$P_L(k, l) = N_L v_{k,l}(k^2 + l^2 + 1)^{\alpha_L/2}. \tag{3.6}$$

In the following numerical experiments on the toy model, we use two independent polarization modes, L_1 and L_2. L_1 and L_2 have different power indexes, α_{L_1} and α_{L_2}, so they have different power spectra. The Gaussian random field here, $g_L(x, y)$ is obtained in a fashion identical to $g(x, y)$, but with independent variables: normalization N_L, power index α_L and realization $v_{k,l}$.

The most significant distinction between the total intensity and the polarization in the way they are generated is that on average, the total polarized intensity vanishes, while the total intensity does not, because the total intensity is built upon a Gaussian distribution whose mean value is non-zero, while the total polarized intensity is generated by multiplying $g_L(x, y)$ whose mean is zero. From the previous discussion about the SSK in Chapter 2, this will naturally suppress the shifting of power from short to long baselines. In the case of the toy model with polarization, as it has zero-mean value, the values of the power spectra at short baselines are tiny, which substantially lessens the contamination from scattering. By using the toy model with polarizations, the ratio of two polarized power spectra exhibit higher fidelity than that from two different unpolarized power spectra, as we will see in the following sections.

3.2 Simulated Observations

Our toy model produces the total intensity map and the different polarization modes corresponding to it. The statistical features of the toy model, including the power spectrum and the total intensity, are controlled by a set of parameters, α, α_{L1}, α_{L2} and I_0. For different realizations of the toy model, there are independently generated fluctuations corresponding to it.

To simulate observations, we must generate scattered images of the toy model. For this, we use the scattering functionality in the EHT-imaging (EHTim) library, which is an imaging producing Python module using VLBI data. The scattering model in the EHTim library is presented in the paper, [6], and is characterized by an inner scale, r_{in}, outer scale, r_{out} and power-law index of the phase fluctuations, α_s.

Applying the EHTim library, we are able to construct an anisotropic scattering screen with random fluctuations. The screen parameters set the scale limit for the scattering procedure. The emission from the accretion disk of Sgr A* changes at the timescale of minutes [21], and the scattering screen varies at the timescale of hours to days [8]. Therefore, for one single EHT observation over one night, we shall have a constant scattering screen with a varying source. For multiple nights of observation, we shall have multiple snapshots, with the varying source and the varying scattering screen. Thus, in our simulation, there are two different types of fluctuations, which needs to be treated separately. The fluctuation in the source simulates the intrinsic fluctuation in the accretion disk, while the fluctuation in the scattering function simulates the time-variability of the scattering screen. The fluctuations are independently generated for each realization of the scattering screen and the intrinsic source. In our simulation, with the screen and source parameters fixed, we pass one realization of the source to one realization of the scattering screen, whose result is called a "snapshot" of the observation. Therefore, for every simulation, both the source and the scattering screen fluctuate independently. The average over many snapshots is the simulation of the ensemble average in the real observation. The procedure is detailed as follows:

1. The first step is to generate the total intensity and its different polarization signals. Following the definition of the total intensity (Equation 3.4) and the add-on fluctuation (Equation 3.3) in Chapter 3.1, we generate the normalized total intensity with fluctuations. Similarly, the polarized signals with zero-mean value can be generated via the definition given in Chapter 3.1 (Equation 3.5). In the simulation, we have different sets of parameter α, α_{L1} and α_{L2}, so the total intensity and the two polarization modes corresponding to it have different features. To make the image,

we set 152 pixels on both axes, and the size of view is 24.4 Schwarzschild radius, which corresponds to 130 μas. The statistics of the add-on fluctuation is that the fluctuation variance is set to be one. For each realization of the source, the source is independently and randomly generated.

2. As the total intensity and all its polarized signals are in the image plane, the next step is to convert them to the visibility plane. By Fourier transforming the total intensity and the polarization maps, i.e., $I(x, y)$, $L_1(x, y)$ and $L_2(x, y)$, we produce the associated intrinsic visibilities, $V_{int,I}$, $V_{int,L1}$ and $V_{int,L2}$, respectively. Note that the EHT covers the baseline up to the size of the Earth, corresponding to 10 Gλ, where $\lambda = 1.3$cm is the observing wavelength. All the figures below will be focusing on the baseline range from 0 to 15 Gλ, which slightly goes beyond the size of the Earth.

3. From the EHTim library, we used the built-in function to generate a scattering screen, fixing parameter values. For our default image simulations, the inner scale and the outer scale are fixed to be 8×10^7 cm and 10^{20} cm respectively, and power-law index of the phase fluctuations α_s is set to be Kolmogorov, 5/3. We ensure that the screen is randomly and independently generated for each realization.

4. For one realization of the intrinsic source, we pass it along to one realization of the scattering screen. Thus we have obtained one snapshot of the scattered images for $I(x, y)$, $L_1(x, y)$ and $L_2(x, y)$.

5. We convert the scattered snapshots into the visibility domain, as we have done in step 2, to obtain the observed visibility ($V_{obs,I}$, $V_{obs,L1}$ and $V_{obs,L2}$).

6. Finally, we repeat this procedure with 100 independently generated intrinsic source and 100 independently generated scattering screen. We take the average of the realizations of both the screen and the intrinsic source to obtain the ensemble average of $V^2_{obs,I}$, $V^2_{obs,L1}$ and $V^2_{obs,L2}$, that is, produce the various power spectra.

Fig. 3.2 shows intrinsic and scattered pictures of both the total intensity and its polarization part. The fluctuation here has a red spectrum, and there are extra substructures introduced by the scattering in both the total intensity picture and polarization picture.

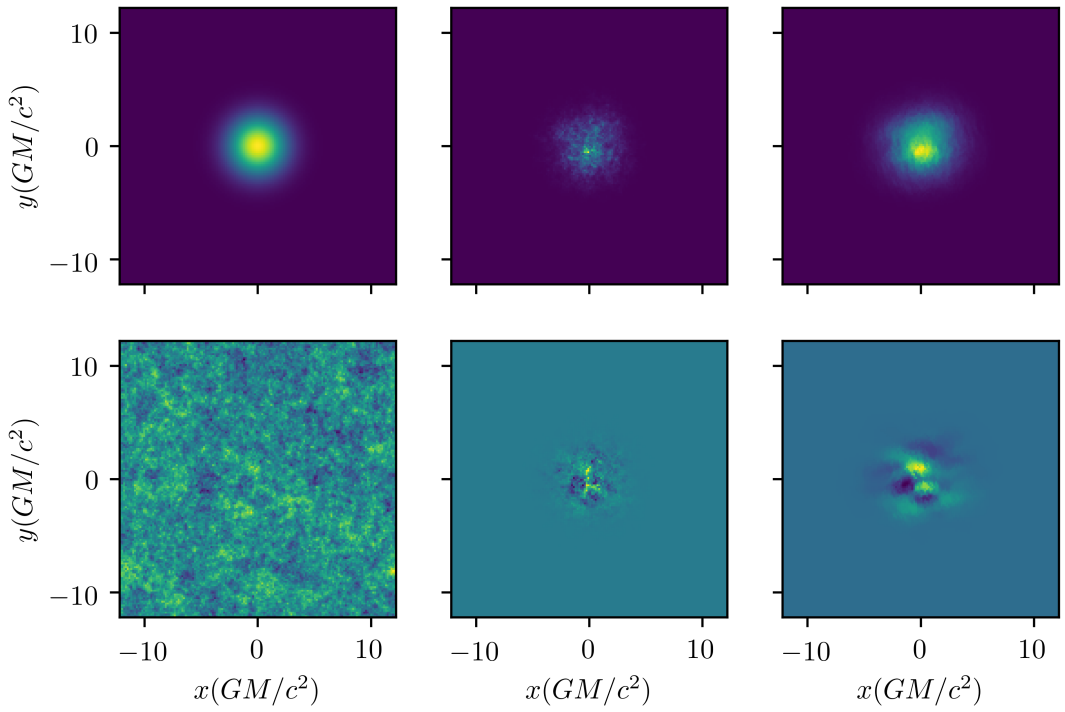

Figure 3.2: The scattered and intrinsic snapshot of the polarized intensity in the toy model. The top row from left to right are the pictures of the total intensity without fluctuation, with fluctuation and scattered intensity with fluctuation. The bottom row from left to right are the pictures of the Gaussian random field that generates the fluctuation g_{L1}, the intrinsic polarized intensity and the scattered polarized intensity.

3.3 Results and Analysis

After setting up the simulated observation, we calculate both the snapshots and ensemble average of the intrinsic and scattered visibility and power spectrum for both total intensity and polarizations.

Table 3.1: Parameter Choice for each Simulation

Type of fluctuations	α	α_L
Blue Total Intensity	2	-
White Total Intensity	0	-
Red Total Intensity	-2	-
L_1	-2	-2
L_2	0	-2

Fig. 3.3 shows the result of the simulation. The top left panel is the power spectra for two different total intensities, whose parameters are listed in Table 3.1 as Blue Total Intensity and Red Total Intensity. Similarly, the top right panel is the power spectra for two different polarization modes listed in Table 3.1, which are L_1 (in the red line) and L_2 (in the blue line). L_2 is based on a white total intensity, with a blue fluctuation in polarization. L_1 is based on a red total intensity , with the same blue fluctuation in polarization. Both the two panels on the top are the ensemble average over 100 realizations on both the screen fluctuation and the intrinsic fluctuation. The solid lines and the dashed lines correspond to intrinsic signals and scattered signal respectively.

In the top right panel, we can see that scattered and intrinsic polarizations preserve the colour of the noise, i.e., preserve the power-law wing with the anticipated colours. In contrast, in the top left panel, we can see that there is bump in the centre for total intensity, which covers the most important information (the preservation of the power law wing) as we read off the top right panel of Fig. 3.3. The reason for this is, as we have discussed in section 3.1, that the total intensity has non-zero mean while polarization has zero mean value. The bump we see in the top left panel of Fig. 3.3 is exactly the bump from Gaussian distribution, $\bar{I}(\mathbf{x})$.

With this in mind, if we calculate the ratio for power spectra between the intrinsic total intensity and its corresponding intrinsic polarization mode, and between the different intrinsic polarization modes before scattering in one chord of the $u - v$ plane. We also calculate the ratio for the scatted quantities in the same way, whose only difference is they

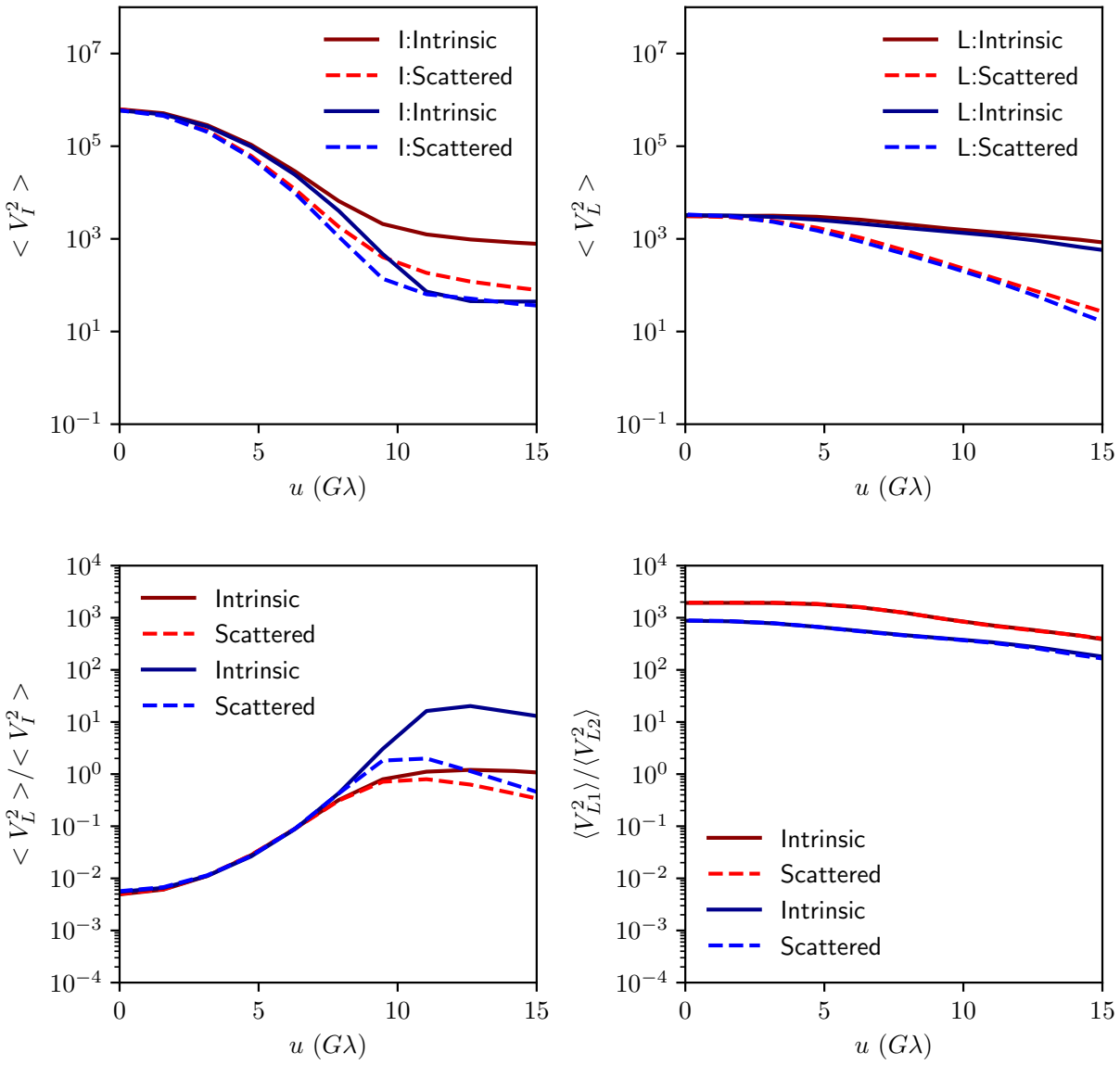

Figure 3.3: The top left panel is the power spectrum of the total intensity before and after scattering. The top right panel is the power spectrum of the polarized signals before and after scattering. The bottom left panel is the ratio of the power spectra between total intensity and polarization. The bottom right is the ratio of the power spectra between two independent polarization modes.

are all after scattering. We find the results shown in the bottom two panels in Fig. 3.3, which we calculate in the u-axis.

In the bottom left panel in Fig. 3.3, we take the ratio of the a polarization component against the total intensity it is based on. The red line corresponds to the ratio between L_1 and the Red Total Intensity in Table 3.1, and the blue line corresponds to the ratio between L_2 and the White Total Intensity in Table 3.1. In the bottom right panel, we take the ratio of two independent polarized signals, L_1 and L_2. The result shows that the ratio for the power law tail after the bump are very close to each other before and after scattering, but there is an obvious deviation. This is because of the SSK we have discussed in Section 2.3.

In the bottom left panel of Fig. 3.3, at short baselines, in the short baseline regime the structure of the ratio is not clear due to the non-zero mean value of the total intensity; however, at longer baselines, we see a deviation. This deviation is a result of the SSK moving the large power at zero-baseline to long baselines. In contrast, the bottom right panel in Fig. 3.3 shows excellent agreement at all baseline lengths. Here, both polarizations have zero-mean values. That is, by carefully choosing the quantities from which we extract structural information so that they have zero means, we drastically improve the fidelity of their power spectra ratios.

Chapter 4

GRMHD simulation

4.1 Constructing the GRMHD model

We now turn to the GRMHD simulation data. The GRMHD images simulates the synchrotron emission in the accretion disk, which provides constraints on the structure and strength of the magnetic field in the accretion disk model, as well as other quantities. Depending on the magnitude of the total magnetic flux in the accretion disk, the GRMHD simulations are divided into two categories, the Standard and Normal Evolution (SANE) and the Magnetically Arrested Disk (MAD) models. In both, depending on the properties of the magnetic field, the scheme of radiative transfer is determined to be either disk model or jet model, which are differentiated by the models for non-thermal electrons [12, 32]. These are approximations of the potential observation data from EHT. Unlike the toy model, we have no control over the intrinsic signals, yet we are able to retrieve key information about intrinsic structures after scattering.

We use the simulated images sets presented in Gold, Mckinney et al. [12]. There are four sets of GRMHD simulation data, MAD disk, MAD jet, SANE disk and SANE jet. All of the simulation data contain the total intensity map and the polarization (both linear and circular), i.e., the four Stokes parameter, I, Q, U and V. Each category of GRMHD data contains at least hundreds, and up to one thousand snapshots of the simulation results of Sgr A*. However, for the GRMHD images we have used, the timespan is relatively short; hence, it might not estimate the full ensemble average. As a result, the shape of the power spectra ratios is not indicative of underlying physical structures. Nevertheless, each GRMHD simulation types is significantly different from each other, and contains very different turbulence properties. In principle, we could apply any accretion disk model of

Sgr A*, as we are not trying to differentiate different accretion disk models, but rather to retrieve information after scattering.

4.2 Simulated Observation

The steps of setting up the simulated observation for GRMHD simulation is similar to the setup procedure in the toy model case. For each GRMHD simulation category separately we:

1. The first step is to generate the total intensity and its corresponding polarization parts. For each GRMHD simulation category, there are four separate data sets, namely the four Stokes parameter (I, Q, U and V). The first parameter, I, encodes the total intensity, and the latter three parameters, Q, U and V, encode three different polarization modes. Similarly, we can construct the polarization so that they have zero-mean value as in the toy model. The detailed method of doing so is described in Section 4.3. Unlike in the toy model, we have no control over the statistical structure of the intrinsic source, as we are now using the GRMHD simulation data.

2. The GRMHD simulation data is converted from the image domain to the visibility domain using the same method in the toy model, i.e., we compute V_{int} for each snapshot in the four polarization modes, $V_{int,I}$, $V_{int,Q}$, $V_{int,U}$, $V_{int,V}$, $V_{int,L1}$ and $V_{int,L2}$. Similarly, the baselines in our later plots in the Chapter covers from 0 to 15 $G\lambda$, at $\lambda = 1.3cm$.

3. We construct the scattering screen from EHTim library with the same parameter configuration as for the toy model.

4. For each snapshot of one GRMHD simulation data category, it is passed through a fixed but independently generated scattering screen with random refractive modes.

5. The scattered intensities are converted from image domain to visibility domain; i.e., we compute V_{scatt} for each snapshot in the four polarization modes, $V_{scatt,I}$, $V_{scatt,Q}$, $V_{scatt,U}$, $V_{scatt,V}$, $V_{scatt,L1}$, $V_{scatt,L2}$.

6. We repeat this procedure until we have covered all the snapshots in one GRMHD simulation data category, and for each snapshot, it is passed through ten independently generated scattering screen.All the parameters in the screen is set to be fixed, leaving the only change in each run of the screen to be some random fluctuation, as a

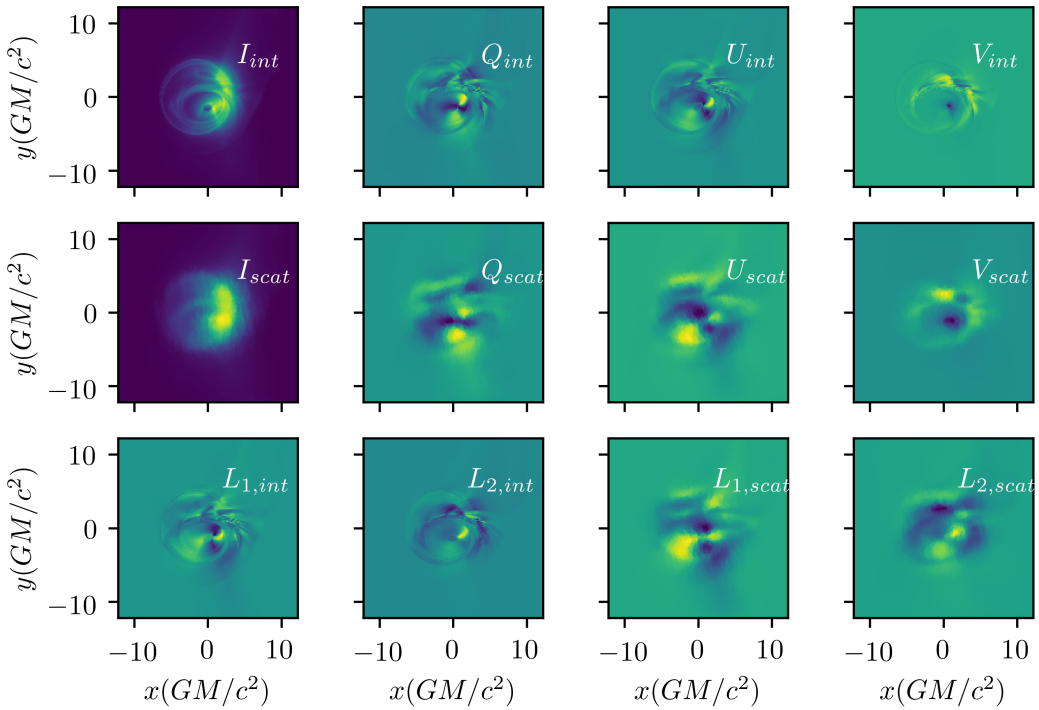

Figure 4.1: The figure shows the images of different polarization modes and their corresponding scattered images. The first line of panels are the intrinsic images for four Stokes parameters, I, Q, U and V. The second line of panels are their corresponding scattered images. The left two panels in the third line are the intrinsic images of the constructed polarization modes, L_1 and L_2, whose mean values are zero. The right two panels in the third line are the corresponding scattered images of L_1 and L_2.

simulation of the intrinsic fluctuation in the screen. Then, we take the ensemble average, as a simulation of the realization of both the fluctuations in the intrinsic source and in the scattering screen to obtain the ensemble average of the power spectrum.

We repeat this for each class of GRMHD data category (SANE jet model, SANE disk model, MAD jet model and MAD disk model), after which we have the statistics for all four GRMHD simulations with the information of polarizations before and after scattering. The intrinsic and scattered image is shown in Fig 4.1.

4.3 Construction of Specific Polarization modes

In the toy model, we have shown that the ratio for scattered power spectra of any two different polarization modes is the same as the ratio for intrinsic power spectra of the same polarization modes, up to the limit of some certain length of baselines. From the discussion in Section 2.2, we know that the SSK, $K(u, b)$, moves power from short baselines to long baselines. Thus, we notice a deviation in the power spectra ratio at shorter baselines, when the mean intensities are large (i.e., large $V(0, 0)$). Thus, the polarization modes are constructed such that they have zero-mean value (zero flux), the scale of baseline limits go beyond the actual size of the Earth, which sets a limit for the current EHT observations. In the toy model, we constructed the two polarization modes with zero-mean value simply by multiplying two independent Gaussian random fields with zero-mean values.

In the GRMHD simulation case, we need to show that the same conclusion holds true in the same way, and we need to find a better way to construct the two polarization modes. To manifest that, we construct the polarization modes in the following way:

1. Present the visibility of the total intensity in the Stokes sphere (Q-U-V) Fig 4.2, $V_{total}(V_Q(0, 0), V_U(0, 0), V_V(0, 0))$
2. Construct the first polarization mode V_{L1} in the Q-U plane such that it is perpendicular to V_{total}.
3. Construct the second polarization mode V_{L_2} such that it is simultaneously perpendicular to both V_{total} and V_{L1}.

As we construct the two polarization modes in the way that V_{L1} and V_{L2} are both perpendicular to the visibility of total intensity V_I in the Stokes Sphere, both V_{L1} and

V_{L2} have zero-mean flux. However, there are infinity many such pairs of V_{L1} and V_{L2} perpendicular to V_{total}. The extra requirement that V_{L1} and V_{L2} are perpendicular to each other gives physical interpretation on the choice of these two polarization modes. Because V_{L1} lives in the Q-U plane, it is the measure of the fluctuation in the linear polarization. Similarly, V_{L2} is the measure of the fluctuation in both the ellipticity. This construction is shown explicitly in Fig 4.2.

4.4 Noise Estimates

The sources of noises are twofold when calculating the ratio of different power spectra with different polarization modes: the thermal noise of the telescope sites and the statistical ensemble average sampling uncertainty due to observation (rms error). Here is the procedure to calculate the two different kinds of noise.

4.4.1 Thermal Noise Estimates

The thermal error is due to the power generated by the resistors in the antenna, which is persistent with non-zero mean value. The standard deviation of the thermal error for one radio telescope is:

$$\sigma_{T1} = \frac{\mathrm{SEFD}_1}{\sqrt{\tau \Delta B}}, \tag{4.1}$$

where τ is the observational time. ΔB is the observational bandwidth, and SEFD is the system equivalent flux density, a measurement of the typical thermal noise in the telescope.

The correlated standard deviation for two different radio telescopes is

$$\sigma_{\langle V \rangle} = \sqrt{\sigma_{T1}\sigma_{T2}}. \tag{4.2}$$

SEFDs for EHT stations are listed in EHTim, ranges from 220 Jy for ALMA to 22000 Jy for APEX. We adopt, for illustration, ALMA and LMT, for which the SEFDs are 220 Jy and 560 Jy, respectively. In our illustration, ALMA and LMT have the two lowest value of SEFDs. If we are to choose different SEFD values for different telescope sites (e.g. SPT with 1600 Jy and SMT with 11900 Jy), the overall estimation of the standard deviation could be raised by one order of magnitude. The value of observational bandwidth and scan time we adopt here are 4 GHz and 10 min.

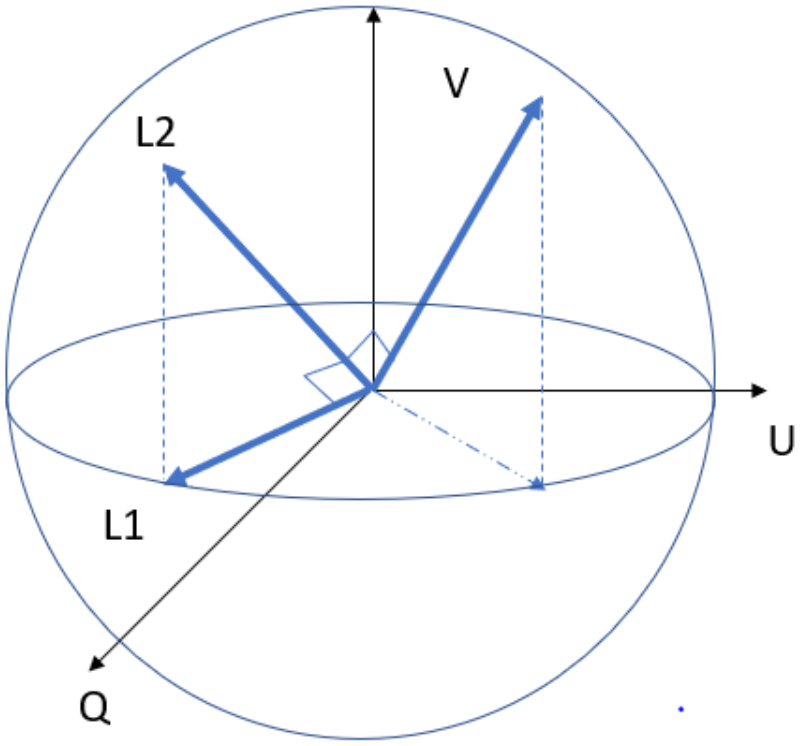

Figure 4.2: The Stokes sphere where V_I, V_{L_1} and V_{L_2} live. The three visibilities are constructed such that they are perpendicular to each other. As V_{L1} and V_{L2} are both perpendicular to the V_I at zero baselines, V_{L1} and V_{L2} have zero-mean values.

The noise can be averaged down by increasing the number of observations, whose standard deviation goes down by $N^{-1/2}$. The standard deviation above is for the $\langle V \rangle$ of any baseline of our choice. The standard deviation for $\langle V^2 \rangle$ can be calculated as follows:

$$\langle V^2 \rangle = \frac{1}{N} \sum_i V_i^2 \tag{4.3}$$

$$\sigma_{\langle V^2 \rangle} = \sqrt{\sum_j \left(\frac{\partial \langle V^2 \rangle}{\partial V_j} \right)^2 \sigma^2_{\langle V \rangle}} \tag{4.4}$$

$$= 2\sqrt{\frac{\langle V^2 \rangle}{N}} \sigma_{\langle V \rangle}. \tag{4.5}$$

As we want to calculate the ratio for power spectra with different polarization modes (e.g., A and B), the standard deviation for the ratio is:

$$\sigma_{\langle V_A^2 \rangle / \langle V_B^2 \rangle} = \frac{\langle V_A^2 \rangle}{\langle V_B^2 \rangle} \sqrt{\left(\frac{\sigma_{\langle V_A^2 \rangle}}{\langle V_A^2 \rangle} \right)^2 + \left(\frac{\sigma_{\langle V_B^2 \rangle}}{\langle V_B^2 \rangle} \right)^2}. \tag{4.6}$$

4.4.2 Ensemble Noise Estimates

The ensemble noise encodes the fluctuation from the turbulence in both the source and the scattering screen.

As stated in the introduction section, the rms error is due to the intrinsic fluctuation in the source and the scattering screen. Unlike the case in the thermal error, the standard deviation of the averaged visibility is polarization mode dependent. The variance of the averaged visibility with different polarization is:

$$\Sigma^2_{\langle V \rangle} = \langle V^2 \rangle - \langle V \rangle^2. \tag{4.7}$$

Thus, the standard deviation for the power spectra ratio is:

$$\Sigma_{\langle V_A^2 \rangle / \langle V_B^2 \rangle} = \frac{\langle V_A^2 \rangle}{\langle V_B^2 \rangle} \sqrt{\left(\frac{\Sigma_{\langle V_A^2 \rangle}}{\langle V_A^2 \rangle} \right)^2 + \left(\frac{\Sigma_{\langle V_B^2 \rangle}}{\langle V_B^2 \rangle} \right)^2}, \tag{4.8}$$

where $\Sigma_{\langle V^2_{A,B} \rangle}$ is the standard deviation from Equation 4.7

4.5 Results and Discussion

Having repeated all the calculations above, we take the ratio of scattered and intrinsic power spectra for different polarization modes in one dimension in one GRMHD data category. As with the toy model, we find it generally possible to faithfully reconstruct the power spectra ratio of polarized observations. In Fig. 4.3 and Fig. 4.4, we take the u-axis as the chord.

In Fig. 4.3 and Fig. 4.4, we show the ratio for polarization mode Q against three other polarization modes I, U and V respectively in all the four GRMHD simulation categories. The error band is the range where the power spectra ratio fluctuates due to the statistical ensemble average sampling uncertainty, while the error bar presents the thermal error from the observational telescope sites. All of the error bars are averaged 25 observational nights.

As is shown in Fig. 4.3 and Fig. 4.4, all of the intrinsic and scattered ratios are indistinguishable from their counterparts at short baselines. For EHT, this result is good enough, as $6-8\ G\lambda$ already covers most of the accessible baselines. However, after this threshold, deviation starts to appear after $6-8\ G\lambda$. The reason for this deviation is exactly the same as in the toy model, as the SSK, $K(u,b)$, moves power from short baselines to long baselines. The ratio between polarization Q and I is the worst among all three ratios against Q, U and V, because the total intensity is two to three orders of magnitude larger than its polarized components; thus, the power moved from short baselines by the SSK is relatively large.

Instead of using the given four polarization modes with the given Stokes parameters, we can use the constructed polarization modes , V_{L1} and V_{L2}, from Section 4.3. As stated in Section 4.3, V_{L_1} and V_{L_2} are chosen in such a way that they have zero-mean value, the contamination from scattering on the power spectra ratio at long baselines is tiny, which is supported by the bottom right panel in Fig. 4.3 and Fig. 4.4, as the power spectra ratio is indistinguishable until over 10 Gλ.

4.6 Screen Sensitivity with the Inner Scale

As we have discussed in the previous chapters that the inner scale and outer scale are the physical scales where the turbulence in the scattering screen is generated and damped respectively. The typical values of inner scale, outer scale and power parameter we used in this numerical experiment are 8×10^7cm, 10^{20}cm and Kolmogorov, 5/3. Arguments do exist on the exact numbers of these values (e.g., see [20]). Some research suggests that the

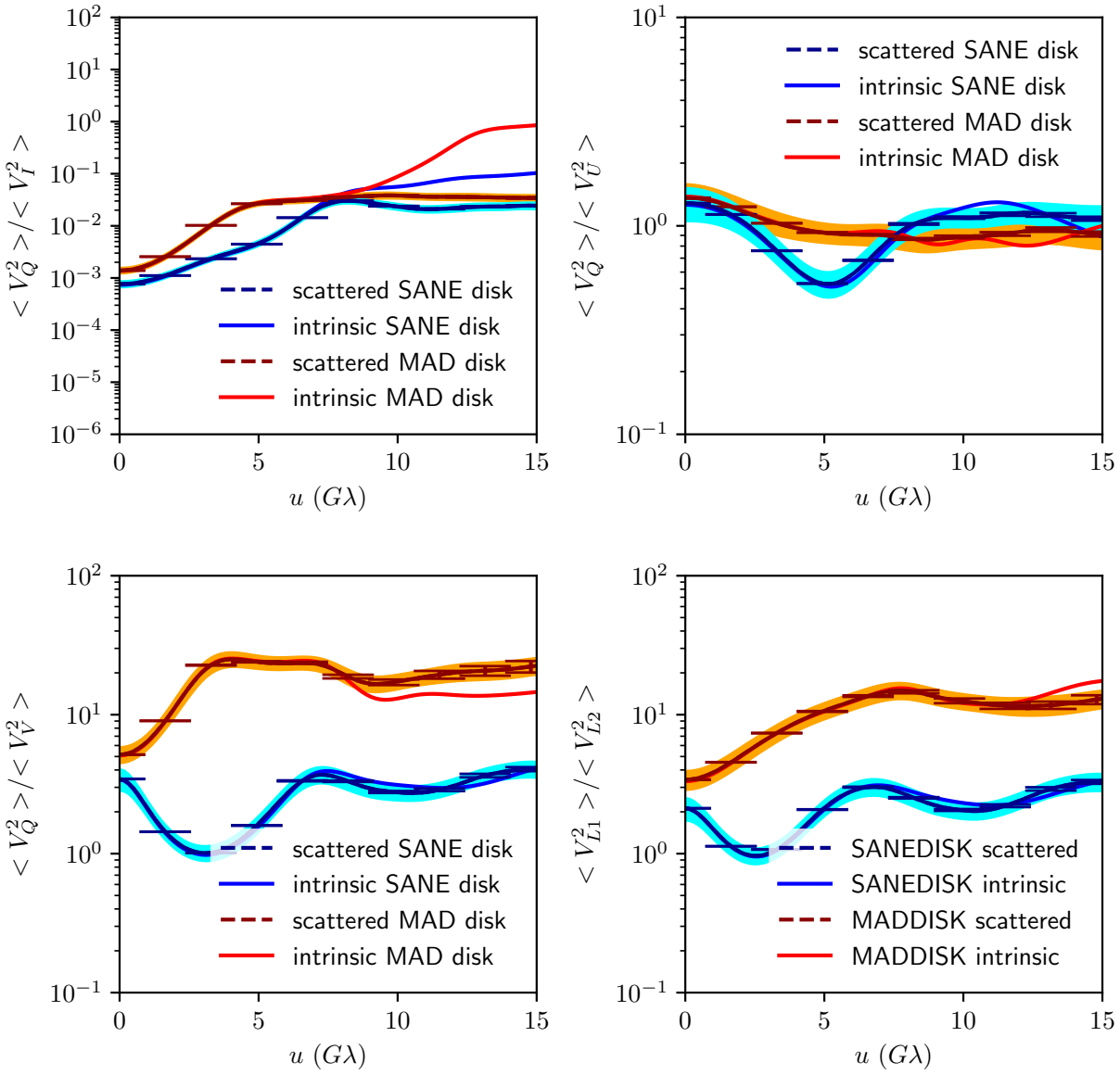

Figure 4.3: The ratio of power spectra for different polarization modes in different disk models, SANE disk model and MAD disk model. The top left, top right and bottom left panels are the ratio of power spectra with Stokes parameter Q over Stokes parameter I, U and V, respectively. The bottom right is the ratio of power spectra with constructed polarization modes V_{L1} and V_{L2}. The error bar is the thermal error, as described in Section 4.4.1, and the error band is the ensemble error, as described in Section 4.4.2

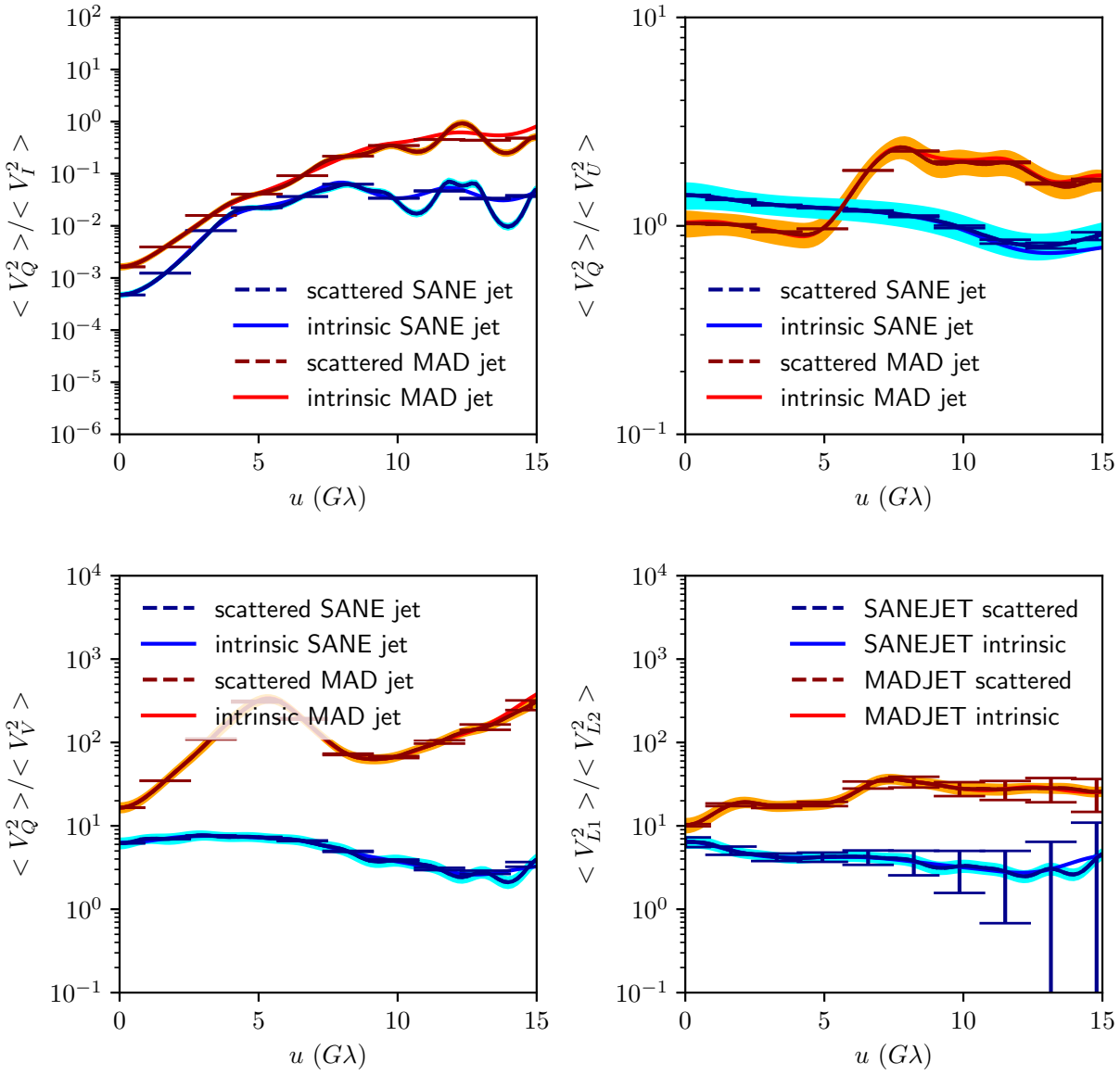

Figure 4.4: The ratio of power spectra for different polarization modes in different jet models, SANE jet model and MAD jet model. he top left, top right and bottom left panels are the ratio of power spectra with Stokes parameter Q over Stokes parameter I, U and V, respectively. The bottom right is the ratio of power spectra with constructed polarization modes V_{L1} and V_{L2}. The error bar is the thermal error, as described in Section 4.4.1, and the error band is the ensemble error, as described in Section 4.4.2

inner scale can be as law as $10^7 cm$, while others suggest that the inner scale can be so large that the entire observation lies within the inner scale. Thus, it is interesting to explore how the power spectra ratio behaves in response to different inner scale values. Within the scattering model in EHTim library, we explored the behaviour of the power spectra ratio for different polarization modes when changing the values of inner scale.

4.6.1 Simulation Results with Different Inner Scales

In this subsection, we present the numerical simulation results with varying scattering the inner scale. We explore the behaviour of the power spectra ratio for different polarization modes in response to different inner scale value, varying from 10^5cm to 10^{13}cm. Three typical values of inner scale were compared, tiny inner scale (e.g. 10^5cm), typical inner scale (e.g. 10^9cm) and large inner scale (e.g. 10^{13}cm), with the test GRMHD simulation data category to be the MAD disk model. The procedure of reconstructing the simulated observation is the same as described in Section 4.2.

The results of the numerical simulation is as follows. First, in the case of the large inner scale, the scattered power spectrum ratio is indistinguishable from the intrinsic ratio. Second, with the intermediate inner scale, as we have presented in the previous section, the scattered power spectrum ratio starts to deviate from the intrinsic power spectrum ratio at long baselines, typically 8 Gλ. Last, with small inner scale, the scatted power spectrum ratio matches the intrinsic ratio again (see Figure 4.5). Therefore, the scattering screen is only sensitive to intermediate inner scales.

4.6.2 Analysis of the Influence of Varying Inner Scale on the Power Spectra Ratios

The result we have acquired from the above numerical simulation shows that the scattering is significant only at intermediate inner scales. When the inner scale is either tiny or large, the scattering effect is not evident. The reason for the case with large inner scale can be directly understood, as all the EHT-accessible baselines are within the inner scale, so the structure function, $D_\phi(\mathbf{r})$, completely falls into the regime of quadratic form. Under this circumstance, the scattered power spectrum is indistinguishable from the instrinsic one (see Equation 2.33). Thus, the power spectrum ratio between different polarization modes is preserved after scattering, even at long baselines.

For the case where the inner scale is intermediate, the structure function would become a piecewise function (See Fig. 2.2): within inner scale it is quadratic, and beyond inner

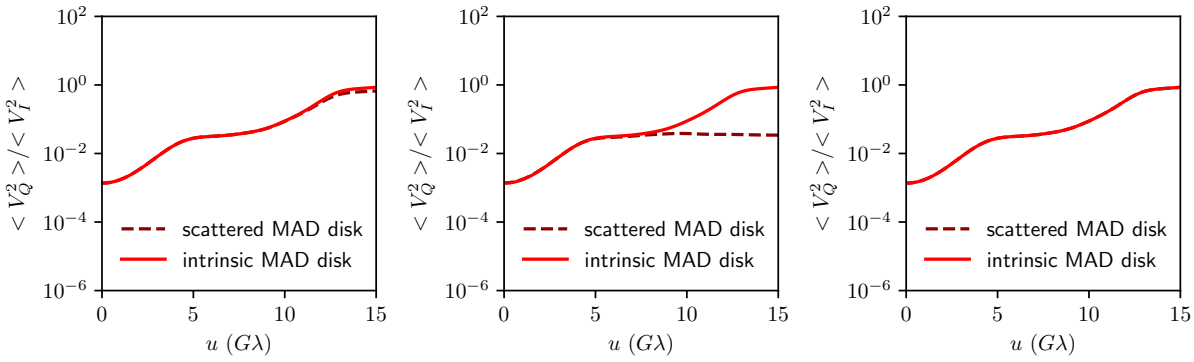

Figure 4.5: These three figures are the power spectrum ratio between Stokes parameter Q and I in the MAD disk model. The difference between these three figures is that they are generated under different inner scales. From left to right, the inner scales are 2×10^5 cm, 10^9 cm and 10^{19} cm.

scale it satisfies power law relation (in this test case, we have chosen the power law to be Kolmogorov). In this case, the scattered power spectrum can be divided into two parts, first of which is proportional to the intrinsic power spectrum, and the second of which is an integration over the SSK (see Equation 2.36 and Equation 2.37). Therefore, the SSK is the reason why we see a deviation of the power spectra ratio at intermediate inner scales.

For the case with tiny inner scale, however, we do not see a deviation of the power spectrum ratio. The reasoning is as follows:

The integrand of Equation 2.37 can be separated into two different parts, the part only as a function of $\mathbf{u}$:

$$K_1(\mathbf{u}) = \frac{1}{2}\mathbf{u}^2 e^{-D_\phi(\mathbf{u})} \langle |V_{int}|^2(\mathbf{u}) \rangle, \tag{4.9}$$

and the part as a function of $\mathbf{z}$:

$$K_2(\mathbf{z}) = e^{i[\mathbf{z}(\mathbf{u}+\mathbf{b})]/r_F^2} D_\phi''(\mathbf{z}). \tag{4.10}$$

There are two limits from these two equations. The first limit is on $\mathbf{u}$ that $e^{-D_\phi(\mathbf{u})}$ exponentially decays when $|\mathbf{u}|$ is too large. This limit on $\mathbf{u}$ is defined as $\bar{\mathbf{u}}$ such that if $|\mathbf{u}| > |\bar{\mathbf{u}}|$, $K_1(\mathbf{u})$ will vanish. The second limit is that the exponent in $K_2(\mathbf{z})$, $e^{i[\mathbf{z}(\mathbf{u}+\mathbf{b})]/r_F^2}$, should be definite and of order one; otherwise, the power spectrum will have violent fluctuations. Thus, $[\mathbf{z}(\mathbf{u}+\mathbf{b})]/r_F^2 < 1$.

There are also two extreme situations here: $|\mathbf{u}| \ll |\mathbf{b}|$ and $|\mathbf{u}| \gg |\mathbf{b}|$. In the first situation, $[\mathbf{z}(\mathbf{u}+\mathbf{b})]/r_F^2 \approx (\mathbf{zb})/r_F^2$, which sets limit on $\mathbf{z}$ that $|\mathbf{z}|_{max} = r_F^2/|\mathbf{b}|$. Similarly, in the second situation, $[\mathbf{z}(\mathbf{u}+\mathbf{b})]/r_F^2 \approx (\mathbf{zu})/r_F^2$, which sets limit on $\mathbf{z}$ that $|\mathbf{z}|_{max} = r_F^2/|\mathbf{u}| > r_F^2/|\bar{\mathbf{u}}|$. This sets constraint of $\mathbf{z}$ on $\mathbf{b}$, based on the value of $\mathbf{u}$, which is shown in Fig 4.6.

As r_{in} is tiny, $|\mathbf{z}|_{max} \gg r_{in}$. In Fig 4.6, $r_{in,2}$ is much smaller than $|\mathbf{z}|_{max}$, which sets a limit on the value of $|\mathbf{b}|$, $|\mathbf{b}|_{max}$. The corresponding limit on $|\mathbf{b}|$, $|\mathbf{b}|_{max}$, is large when r_{in} is tiny. Within this limit of $|\mathbf{b}|$, the power spectrum is not affected by the scattering.

Fig 4.6 shows two cases, $r_{in,1}$ corresponds to intermediate inner scale, and $r_{in,2}$ corresponds to tiny inner scale. For $r_{in,1}$, once it moves out of $|\mathbf{b}|_{max,1}$, the inner scale is larger than $|\mathbf{z}|_{max}$, and the SSK starts to contaminate the power spectrum; thus, the scattered power spectrum starts to deviate from the intrinsic one at certain baselines. Similarly, as $r_{in,2}$ is much smaller than $r_{in,1}$, the corresponding limit on $|\mathbf{b}|$, $|\mathbf{b}|_{max,2}$ is much larger than $|\mathbf{b}|_{max,1}$; hence, the deviation of the scattered power spectrum ratio happens at much longer baselines. Therefore, the deviation of the scattered power spectrum cannot be observed at the EHT-accessible baselines in Fig 4.5.

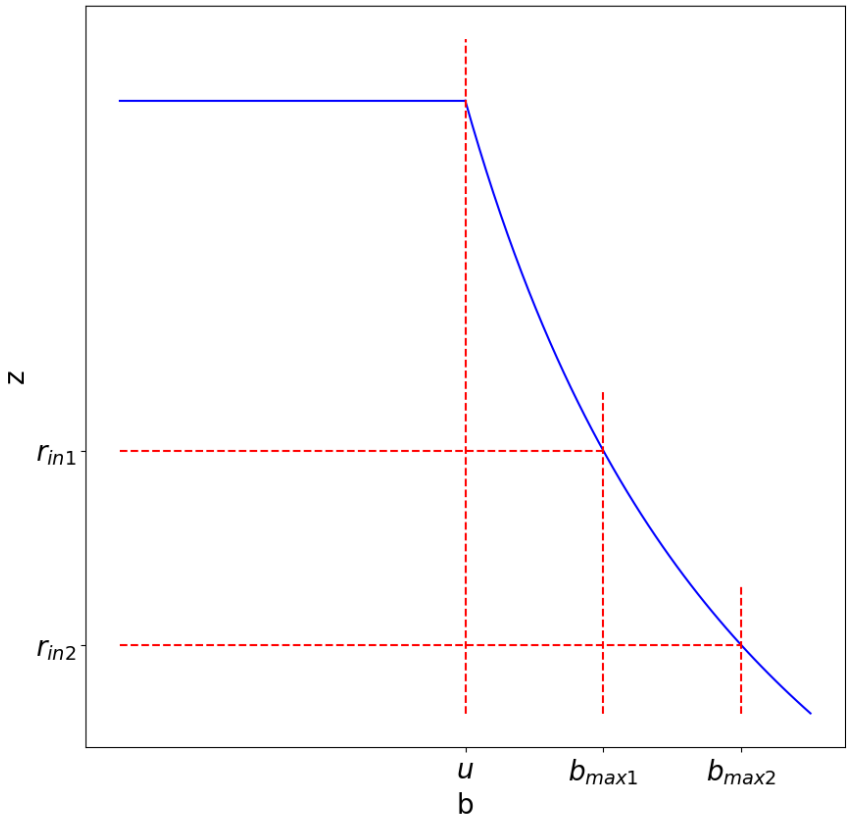

Figure 4.6: The plot shows the constraint of $\mathbf{z}$ on $\mathbf{b}$. The top left plateau happens when $\mathbf{u} \gg \mathbf{b}$, while the right curve happens when $\mathbf{u} \ll \mathbf{b}$. For a given inner scale smaller than $|\mathbf{z}|_{max}$, there is a corresponding upper limit $|\mathbf{b}|_{max}$ such that within the baseline $|\mathbf{b}|_{max}$, the power spectrum is not affected by the scattering.

Chapter 5

Conclusion

5.1 Current Conclusions

We have reached four main conclusions based on our exploration of methods to mitigate interstellar scattering using polarization observations.

First, the interstellar scattering is generally non-birefringent. To observe a distinctive difference among different polarizations after interstellar scattering, a magnetic field at least 10^7 mG is required, much larger than any credible estimates of the magnetic field strengths in the interstellar medium. Therefore, key aspects of the relative information between different polarization modes is preserved even after scattering.

Second, the SSK that we have defined characterizes the influence of scattering on the power spectrum of intensity fluctuations within images (in all Stokes parameters). We find that typically the SSK shifts power from short baselines to long baselines, i.e., large angular scales to small angular scales, which contaminates the power spectra of image fluctuations. This is true for all Stokes parameters. However, for a wide range of potential scattering screen properties, the ratios of power spectra for appropriately defined polarization quantities are only weakly affected.

Third, based on the numerical simulations using toy models, we have confirmed explicitly that the statistical information of the intrinsic image structure is preserved after scattering. The ratio for power spectra produced from different polarizations is indistinguishable before and after scattering. This match between the statistical description of observed and intrinsic image structure is significantly improved when polarization modes are constructed to have zero-mean values, mitigating the contamination from the SSK.

Last, using numerical simulations of images produced from GRMHD simulation data, we demonstrated the ability of polarimetric power spectra ratios to convey practical information about the underlying intrinsic image structure for realistic scenarios. Testing out different combinations of polarization modes in four different intrinsic GRMHD simulation data categories, the ratio of the scattered power spectra is still closely matched to the ratio of the intrinsic ones, up to long baselines. If constructing the polarized signals (L_1 and L_2) with polarization modes chosen such that total L_1 and L_2 have zero-mean value, we can substantially reduce the contamination from scattering via the SSK. Physically, these two finely constructed polarized signals characterize the fluctuation in the linear and elliptical polarizations. Differences among the power spectra ratios for different underlying models, indicative of the range we may anticipate from different models of MHD turbulence, continue to be clearly distinguishable even when thermal and ensemble noise are included for typical EHT observations.

5.2 Future Plans

Motivated by the success of our attempts to mitigate interstellar scattering with polarimetric observations, there are a number of natural future projects. These focus on extending, characterizing, and applying the results of this thesis.

First, while we have shown that intrinsic information may be robustly reconstructed, the implication of a given power spectra ratio remains to be understood physically. For the numerical experiments we have performed using the GRMHD simulation data, the power spectra ratios are very distinct. However, it is unclear how much of this is a result of the short run time (and thus lack of independent intrinsic image realizations) and how much is indicative of the MHD turbulence. This can be explored using both longer-time GRMHD simulations, and more accurate toy models that utilize structured emission regions and fully general relativistic ray tracing.

Second, we have developed the ability to access intrinsic information about the spatial power spectrum of fluctuations in the emission region. However, more powerful would be a measure of the full spatiotemporal power spectrum. Currently, our method effectively produces the spatial power spectrum at zero time lag. In the future we will explore the prospects for producing estimates of the spatial power spectra that include temporal structure that are robust to scattering.

Third, and perhaps most important, is the application of this to existing and forthcoming EHT observations. In 2017, 2018 and expected in 2019, the EHT observed the full

set of Stokes parameters. This has been supplemented with a large library of GRMHD simulations. The calibration and analysis of this data is currently underway, and we expect to apply the methods developed here to both the observations and simulation library, addressing the self-consistency of modern accretion models of Sgr A*.

References

[1] Steven A. Balbus and John F. Hawley. Instability, turbulence, and enhanced transport in accretion disks. *Reviews of Modern Physics*, 70:1–53, January 1998.

[2] Amitai Y. Bin-Nun. Strong gravitational lensing by Sgr A*. *Classical and Quantum Gravity*, 28:114003, June 2011.

[3] RD Blandford and DG Payne. Hydromagnetic flows from accretion discs and the production of radio jets. *Monthly Notices of the Royal Astronomical Society*, 199(4):883–903, 1982.

[4] A. Boehle, A. M. Ghez, R. Schödel, L. Meyer, S. Yelda, S. Albers, G. D. Martinez, E. E. Becklin, T. Do, J. R. Lu, K. Matthews, M. R. Morris, B. Sitarski, and G. Witzel. An improved distance and mass estimate for sgr a* from a multistar orbit analysis. *The Astrophysical Journal*, 830(1):17, 2016.

[5] Avery E. Broderick, Vincent L. Fish, Michael D. Johnson, Katherine Rosenfeld, Carlos Wang, Sheperd S. Doeleman, Kazunori Akiyama, Tim Johannsen, and Alan L. Roy. Modeling Seven Years of Event Horizon Telescope Observations with Radiatively Inefficient Accretion Flow Models. *apj*, 820:137, April 2016.

[6] Andrew A. Chael, Michael D. Johnson, Ramesh Narayan, Sheperd S. Doeleman, John F. C. Wardle, and Katherine L. Bouman. High-resolution Linear Polarimetric Imaging for the Event Horizon Telescope. *apj*, 829:11, September 2016.

[7] J. Dexter, A. Deller, G. C. Bower, P. Demorest, M. Kramer, B. W. Stappers, A. G. Lyne, M. Kerr, L. G. Spitler, D. Psaltis, M. Johnson, and R. Narayan. Locating the intense interstellar scattering towards the inner Galaxy. *mnras*, 471:3563–3576, November 2017.

[8] Vincent L. Fish, Michael D. Johnson, Ru-Sen Lu, Sheperd S. Doeleman, Katherine L. Bouman, Daniel Zoran, William T. Freeman, Dimitrios Psaltis, Ramesh Narayan,

Victor Pankratius, Avery E. Broderick, Carl R. Gwinn, and Laura E. Vertatschitsch. Imaging an Event Horizon: Mitigation of Scattering toward Sagittarius A*. *apj*, 795:134, November 2014.

[9] Juhan Frank, Andrew King, and Derek Raine. *Accretion power in astrophysics*. Cambridge university press, 2002.

[10] Steven B. Giddings and Dimitrios Psaltis. Event Horizon Telescope observations as probes for quantum structure of astrophysical black holes. *prd*, 97:084035, April 2018.

[11] S. Gillessen, F. Eisenhauer, S. Trippe, T. Alexander, R. Genzel, F. Martins, and T. Ott. Monitoring stellar orbits around the massive black hole in the galactic center. *The Astrophysical Journal*, 692(2):1075, 2009.

[12] Roman Gold, Jonathan C. McKinney, Michael D. Johnson, and Sheperd S. Doeleman. Probing the Magnetic Field Structure in Sgr A* on Black Hole Horizon Scales with Polarized Radiative Transfer Simulations. 837:180, March 2017.

[13] J. Goodman and R. Narayan. The Shape of a Scatter Broadened Image - Part Two - Interferometric Visibilities. *mnras*, 238:995, June 1989.

[14] Gravity Collaboration, R. Abuter, A. Amorim, M. Bauboeck, J. P. Berger, H. Bonnet, W. Brandner, Y. Clenet, V. Coude Du Foresto, P. T. de Zeeuw, C. Deen, J. Dexter, G. Duvert, A. Eckart, F. Eisenhauer, N. M. Foerster Schreiber, P. Garcia, F. Gao, E. Gendron, R. Genzel, S. Gillessen, P. Guajardo, M. Habibi, X. Haubois, T. Henning, S. Hippler, M. Horrobin, A. Huber, A. Jimenez-Rosales, L. Jocou, P. Kervella, S. Lacour, V. Lapeyrere, B. Lazareff, J. B. Le Bouquin, P. Lena, M. Lippa, T. Ott, J. Panduro, T. Paumard, K. Perraut, G. Perrin, O. Pfuhl, P. M. Plewa, S. Rabien, G. Rodriguez-Coira, G. Rousset, A. Sternberg, O. Straub, C. Straubmeier, E. Sturm, L. J. Tacconi, F. Vincent, S. von Fellenberg, I. Waisberg, F. Widmann, E. Wieprecht, E. Wiezorrek, J. Woillez, and S. Yazici. VizieR Online Data Catalog: SgrA* orbital motions with GRAVITY (GRAVITY Collaboration, 2018). *VizieR Online Data Catalog*, pages J/A+A/618/L10, November 2018.

[15] C. R. Gwinn, M. C. Britton, J. E. Reynolds, D. L. Jauncey, E. A. King, P. M. McCulloch, J. E. J. Lovell, and R. A. Preston. Interstellar optics. *The Astrophysical Journal*, 505(2):928, 1998.

[16] C. R. Gwinn, Y. Y. Kovalev, M. D. Johnson, and V. A. Soglasnov. Discovery of Substructure in the Scatter-broadened Image of Sgr A*. *apj*, 794:L14, October 2014.

[17] Igor V. Igumenshchev, Ramesh Narayan, and Marek A. Abramowicz. Three-dimensional Magnetohydrodynamic Simulations of Radiatively Inefficient Accretion Flows. 592:1042–1059, August 2003.

[18] Michael D. Johnson and Carl R. Gwinn. Theory and simulations of refractive substructure in resolved scatter-broadened images. *The Astrophysical Journal*, 805(2):180, 2015.

[19] Michael D. Johnson and Ramesh Narayan. The Optics of Refractive Substructure. *apj*, 826:170, August 2016.

[20] Michael D. Johnson, Ramesh Narayan, Dimitrios Psaltis, Lindy Blackburn, Yuri Y. Kovalev, Carl R. Gwinn, Guang-Yao Zhao, Geoffrey C. Bower, James M. Moran, Motoki Kino, Michael Kramer, Kazunori Akiyama, Jason Dexter, Avery E. Broderick, and Lorenzo Sironi. The Scattering and Intrinsic Structure of Sagittarius A* at Radio Wavelengths. *apj*, 865:104, October 2018.

[21] Ru-Sen Lu, Freek Roelofs, Vincent L. Fish, Hotaka Shiokawa, Sheperd S. Doeleman, Charles F. Gammie, Heino Falcke, Thomas P. Krichbaum, and J. Anton Zensus. Imaging an Event Horizon: Mitigation of Source Variability of Sagittarius A*. *apj*, 817:173, February 2016.

[22] Ramesh Narayan and Jeremy Goodman. The shape of a scatter-broadened image. I - Numerical simulations and physical principles. *mnras*, 238:963–1028, June 1989.

[23] Ramesh Narayan, Igor V. Igumenshchev, and Marek A. Abramowicz. Magnetically Arrested Disk: an Energetically Efficient Accretion Flow. *Publications of the Astronomical Society of Japan*, 55:L69–L72, December 2003.

[24] Ramesh Narayan, Aleksander SÄ dowski, Robert F. Penna, and Akshay K. Kulkarni. GRMHD simulations of magnetized advection-dominated accretion on a non- spinning black hole: role of outflows. 426:3241–3259, November 2012.

[25] Martin E. Pessah. Angular Momentum Transport in Protoplanetary and Black Hole Accretion Disks: The Role of Parasitic Modes in the Saturation of MHD Turbulence. 716:1012–1027, June 2010.

[26] Dimitrios Psaltis. Testing General Relativity with the Event Horizon Telescope. *ArXiv e-prints*, page arXiv:1806.09740, June 2018.

[27] Dimitrios Psaltis, Feryal Özel, Chi-Kwan Chan, and Daniel P. Marrone. A General Relativistic Null Hypothesis Test with Event Horizon Telescope Observations of the Black Hole Shadow in Sgr A*. *apj*, 814:115, December 2015.

[28] Sean M Ressler, Alexander Tchekhovskoy, Eliot Quataert, and Charles F Gammie. The disc-jet symbiosis emerges: modelling the emission of sagittarius a* with electron thermodynamics. *Monthly Notices of the Royal Astronomical Society*, 467(3):3604–3619, 2017.

[29] Benjamin R. Ryan, Charles F. Gammie, Sebastien Fromang, and Pierre Kestener. Resolution Dependence of Magnetorotational Turbulence in the Isothermal Stratified Shearing Box. *apj*, 840:6, May 2017.

[30] Rajibul Shaikh, Prashant Kocherlakota, Ramesh Narayan, and Pankaj S. Joshi. Shadows of spherically symmetric black holes and naked singularities. *mnras*, 482:52–64, January 2019.

[31] N. I. Shakura and R. A. Sunyaev. Black holes in binary systems. Observational appearance. 500:33–51, June 2009.

[32] Aleksander Sadowski, Ramesh Narayan, Robert Penna, and Yucong Zhu. Energy, momentum and mass outflows and feedback from thick accretion discs around rotating black holes. *mnras*, 436:3856–3874, December 2013.

[33] Steven R. Spangler and Carl R. Gwinn. Evidence for an Inner Scale to the Density Turbulence in the Interstellar Medium. 353:L29, April 1990.

[34] Lyman Spitzer. *Physics of fully ionized gases*. Courier Corporation, 2006.

[35] Alexander Tchekhovskoy, Ramesh Narayan, and Jonathan C. McKinney. Efficient generation of jets from magnetically arrested accretion on a rapidly spinning black hole. 418:L79–L83, November 2011.

[36] A. Richard Thompson, James M. Moran, and Jr. Swenson, George W. *Interferometry and Synthesis in Radio Astronomy, 2nd Edition*. 2001.

APPENDICES

Appendix A

Calculating of visibility, power spectrum and variance with scalar light approximation

For an extended source with scalar light approximation, the electromagnetic wave is:

$$\Psi(\vec{b}) = \frac{1}{2\pi r_F^2} \int_{screen} d^2\vec{x} \times e^{i[(\frac{k}{2D})|\vec{b}-\vec{x}|^2+\phi(\vec{x})]} \times \int_{src} d^2\vec{s} e^{i(\frac{k}{2R})|\vec{x}-\vec{s}|^2} \Psi_{src}(\vec{s}).$$

The corresponding visibility for this electromagnetic wave with arbitrary polarization AB is:

$$V_{AB,obs}(\vec{b}) = \frac{1}{4\pi^2 r_F^4} \int d^2\vec{x_1} d^2\vec{x_2} \times e^{i\frac{1}{2}r_F^{-2}[(x_1^2-x_2^2)+\frac{\vec{b}}{1+M}(\vec{x_1}+\vec{x_2})]} \times e^{i[\phi(\vec{x_1})-\phi(\vec{x_2})]} V_{AB,int}((1+M)(\vec{x_2}-\vec{x_1})).$$

The source has intrinsic structure, i.e. variance, so we can take two averages for an extended source: the turbulence average and the screen average. The turbulence average of the

visibility is:

$$\langle V_{AB,obs}(\vec{b})\rangle_{turb} = \frac{1}{4\pi^2 r_F^4}\int d^2\vec{x_1}d^2\vec{x_2}$$
$$\times e^{i\frac{1}{2}r_F^{-2}[(x_1^2-x_2^2)+\frac{\vec{b}}{1+M}(\vec{x_1}+\vec{x_2})]}$$
$$\times e^{i[\phi(\vec{x_1})-\phi(\vec{x_2})]}\langle V_{AB,int}((1+M)(\vec{x_2}-\vec{x_1}))\rangle_{turb}.$$

The square of the visibility is:

$$V_{AB,obs}^2(\vec{b}) = \frac{1}{(4\pi^2 r_F^4)^2}\int d^2\vec{x_1}d^2\vec{x_2}d^2\vec{x_3}d^2\vec{x_4}$$
$$\times e^{i\frac{1}{2}r_F^{-2}[(x_1^2-x_2^2)+\frac{\vec{b}}{1+M}(\vec{x_1}+\vec{x_2})-(x_3^2-x_4^2)-\frac{\vec{b}}{1+M}(\vec{x_3}+\vec{x_4})]}$$
$$\times e^{i[\phi(\vec{x_1})-\phi(\vec{x_2})-\phi(\vec{x_3})+\phi(\vec{x_4})]}$$
$$V_{AB,int}((1+M)(\vec{x_2}-\vec{x_1}))V_{AB,int}((1+M)(\vec{x_4}-\vec{x_3})).$$

Then, we can take the turbulence average of the squared visibility:

$$\langle V_{AB,obs}^2\rangle_{turb} = \frac{1}{(4\pi^2 r_F^4)^2}\int d^2\vec{x_1}d^2\vec{x_2}d^2\vec{x_3}d^2\vec{x_4}$$
$$\times e^{i\frac{1}{2}r_F^{-2}[(x_1^2-x_2^2)+\frac{\vec{b}}{1+M}(\vec{x_1}+\vec{x_2})-(x_3^2-x_4^2)-\frac{\vec{b}}{1+M}(\vec{x_3}+\vec{x_4})]}$$
$$\times e^{i[\phi(\vec{x_1})-\phi(\vec{x_2})-\phi(\vec{x_3})+\phi(\vec{x_4})]}$$
$$\times[\sigma^2((1+M)(x_2-x_1),(1+M)(x_4-x_3))$$
$$+\langle V_{AB,int}((1+M)(\vec{x_2}-\vec{x_1}))\rangle\times\langle V_{AB,int}((1+M)(\vec{x_4}-\vec{x_3}))\rangle],$$

where σ is:

$$\sigma^2(x_2-x_1,x_4-x_3) = \langle V(1+M)(x_2-x_1)V(1+M)(x_4-x_3)\rangle$$
$$-\langle V(1+M)(x_2-x_1)\rangle\langle V(1+M)(x_4-x_3)\rangle$$

We will later see that x_2-x_1 has to be the same as x_4-x_3 to have non-zero σ In order to simplify it, we apply the following change of variables:

$$\begin{bmatrix} z_1 \\ z_2 \\ z_3 \\ z_4 \end{bmatrix} = \frac{1}{2}\begin{bmatrix} 1 & 1 & 1 & 1 \\ 1 & -1 & 1 & -1 \\ 1 & 1 & -1 & -1 \\ 1 & -1 & -1 & 1 \end{bmatrix}\begin{bmatrix} x_1 \\ x_2 \\ x_3 \\ x_4 \end{bmatrix}$$

Two identities which are going to be used are:

$$z_2 + z_4 = x_1 - x_2$$
$$z_4 - z_2 = x_4 - x_3.$$

The first term in the turbulence average of the squared visibility is:

$$\begin{aligned}
\langle \mathrm{firstterm} \rangle_{\mathrm{turb}} &= \frac{1}{(4\pi^2 \mathrm{r_F^4})^2} \int \mathrm{d^2 z_i} \\
&\times e^{i r_F^{-2} [z_1 z_4 + z_2 z_3 + \frac{b}{1+M} z_3]} \\
&\times e^{i\phi} \times \sigma^2[-(1+M)(z_2+z_4)] \\
&= \frac{1}{4\pi^2 r_F^4} \int d^2 z_2 d^2 z_3 d^2 z_4 \\
&\times e^{i r_F^{-2} [z_2 z_3 + \frac{b}{1+M} z_3]} \\
&\times e^{i\phi} \times \sigma^2[-(1+M)(z_2+z_4)] \delta(z_4) \\
&= \frac{1}{4\pi^2 r_F^4} \int d^2 z_2 d^2 z_3 \\
&\times e^{i r_F^{-2} [z_2 z_3 + \frac{b}{1+M} z_3]} \\
&\times e^{i[\phi(\frac{1}{2}(z_1+z_2+z_3)) - \phi(\frac{1}{2}(z_1-z_2+z_3)) - \phi(\frac{1}{2}(z_1+z_2-z_3)) + \phi(\frac{1}{2}(z_1-z_2-z_3))]} \\
&\times \sigma^2[-(1+M) z_2].
\end{aligned}$$

Then we can take the screen average, the only term to do with the screen is the phase change ϕ. And also, if we take result that z_4 equals 0, then we can relate the change of the phase to the correlation function:

$$\left\langle e^{i[\phi(x_1) - \phi(x_2)]} \right\rangle_{ea} = e^{-\frac{1}{2}\langle [\phi(x_1) - \phi(x_2)]^2 \rangle_{ea}} = e^{-\frac{1}{2} D_\phi (x_1 - x_2)}.$$

So, the first term is after taking two averages is:

$$\begin{aligned}
\langle firstterm \rangle_{turb,ea} &= \frac{1}{4\pi^2 r_F^4} \int d^2 z_2 d^2 z_3 \\
&\times e^{i r_F^{-2} [z_2 z_3 + \frac{b}{1+M} z_3]} \\
&\times e^{-\frac{1}{2}[2D_\phi(z_2) + 2D_\phi(z_3) - D_\phi(z_2+z_3) - D_\phi(-z_2+z_3)]} \\
&\times \sigma^2[-(1+M) z_2].
\end{aligned}$$

If we take the approximation that:

$$D_\phi(x) = \frac{x^2}{r_0^2}.$$

Then,

$$\begin{aligned}\langle \text{firstterm} \rangle_{\text{turb,ea}} = \frac{1}{4\pi^2 \mathrm{r}_\mathrm{F}^4} \int \mathrm{d}^2\mathrm{z}_2 \mathrm{d}^2\mathrm{z}_3 \\ \times e^{i r_F^{-2}[z_2 z_3 + \frac{b}{1+M} z_3]} \\ \times \sigma^2[-(1+M)z_2] \\ = \sigma^2(b).\end{aligned}$$

Following the same logic, we can calculate the second term as follows:

$$\begin{aligned}\langle \text{secondterm} \rangle_{\text{turb,ea}} = \frac{1}{(4\pi^2 \mathrm{r}_\mathrm{F}^4)^2} \int \mathrm{d}^2\mathrm{z}_\mathrm{i} \\ e^{i r_F^{-2}(z_1 z_4 + z_2 z_3 + \frac{b}{1+M} z_3)} \times e^{-2\frac{z_4^2}{r_0^2}} \\ \times \langle V_{AB,int}(-(1+M)(z_2+z_4)) \rangle_{turb} \langle V_{AB,int}(-(1+M)(z_2-z_4)) \rangle_{turb} \\ = \langle V_{AB,int}(b) \rangle_{turb}^2.\end{aligned}$$

So,

$$\langle V_{AB,obs}^2(b) \rangle_{ea,turb} = \sigma^2(b) + \langle V_{AB,int}(b) \rangle_{turb}^2 = \langle V_{AB,int}^2(b) \rangle_{ea,turb}.$$

If we apply the same logic to the average of visibility instead of visibility squared, we would have:

$$\langle V_{AB}(b) \rangle_{ea,turb} = e^{-\frac{1}{2}\frac{b^2}{(1+M)^2}\frac{1}{r_0^2}} \langle V_{AB}(b) \rangle_{turb}.$$

Therefore, the variance can be written as:

$$\Sigma^2(b) = \sigma^2(b) + (1 - e^{-\frac{b^2}{(1+M)^2}\frac{1}{r_0^2}}) \langle V_{AB}(b) \rangle_{turb}.$$